



Cairo University



Horus II



AIAA Design | Build | Fly 20-21
Design Report

Table of Contents

List of Figures	2
List of Tables	4
Acronyms, Abbreviations, and Symbols.....	5
1.0 Executive Summary	6
1.1 Design Process.....	6
1.2 Performance and Capabilities of the Design.....	6
2.0 Management Summary	7
2.1 Team Organization	7
2.2 Management Chart	7
2.3 Milestone Chart.....	8
3.0 Conceptual Design.....	9
3.1 Mission Requirements	9
3.2 Design Requirements	12
3.3 Configuration Selection.....	14
3.4 Final Conceptual Design.....	19
4.0 Preliminary Design.....	19
4.1 Design Methodology	20
4.2 Mission Model.....	20
4.3 Design Trades.....	22
4.4 Aerodynamic Characteristics	23
4.5 Stability and Control.....	28
4.6 Mission Performance Estimations.....	32
5.0 Detailed Design	33
5.1 Dimensional Parameters.....	33
5.2 Structural Characteristics and Capabilities	34
5.3 Subsystems Design	35
5.4 Weight and Balance.....	39
5.5 Flight and Mission Performance.....	41
5.6 Drawing Package.....	41
6.0 Manufacturing Plan	46
6.1 Manufacturing Process Investigated	46
6.2 Selected Manufacturing Process	48
6.3 Manufacturing Schedule	50
7.0 Testing Plan	50
7.1 Testing Schedule and Objectives.....	51
7.2 Subsystem Testing	51
7.3 Ground Mission Simulation	54
7.4 Flight Testing	55
7.5 Flight Checklists	55
8.0 Performance Results	56
8.1 Demonstrated Performance of Key Subsystems	56
9.0 Bibliography	58

List of Figures

Figure 1.1: The Final Aircraft (Horrus II).....	6
Figure 2.1: Team Structure.....	7
Figure 2.2: Milestone Gantt Chart	8
Figure 2.3: Post Lockdown Milestone.....	8
Figure 3.1: Course Layout	9
Figure 3.2: Estimated Score of Various Design Scenarios	13
Figure 3.4: The First Sensor Configuration	18
Figure 3.4: The Second Sensor Configuration	18
Figure 3.6: First Mechanism	19
Figure 3.6: Second Mechanism.....	19
Figure 3.7: Final Conceptual Design	19
Figure 4.1: Flow Chart of the Team Design Methodology.....	20
Figure 4.2: Flight Course Model	20
Figure 4.3: Matching Plot.....	22
Figure 4.4: The Selected Airfoil	24
Figure 4.5: s3002 Performance	24
Figure 4.6: Flap Effect on the Lift Coefficient	25
Figure 4.7: Parasite Drag Pie-chart.....	26
Figure 4.8: Drag Polar Estimation	27
Figure 4.9: Pressure Contour of the Aircraft.....	27
Figure 4.10: Pressure Contour of the Sensor.....	27
Figure 4.11: Horizontal and Vertical Tail Dimensions	28
Figure 4.12: C_m Versus α Curve	30
Figure 4.13: Pole-Zero Diagram	30
Figure 4.14: Time Response Plots	31
Figure 5.1: Load Paths of Major Forces	34
Figure 5.2: Flight Envelope Diagram	35
Figure 5.3: Wing Structure.....	35
Figure 5.4: Fuselage Interior Structure.....	36
Figure 5.5: Landing Gear Design	36
Figure 5.6: Tail Assembly	37
Figure 5.7: Selected Servos	37
Figure 5.8: Sensor Design.....	37
Figure 5.9: Deploying/Recovery Mechanism.....	38
Figure 5.10: Container Design.....	38

Figure 5.11: Available and Required Thrust for Each Mission	39
Figure 6.1: Wing and Fuselage Fixation.....	48
Figure 6.2: Tail Assembly	48
Figure 6.3: Deployment/recovery mechanism	48
Figure 6.4: Fuselage Structure	49
Figure 6.5: The Sensor Fixation Inside its Shipping Container	49
Figure 6.6: The Towed Sensor Structure	49
Figure 6.7: Manufacturing Milestone	50
Figure 7.1: Testing Plan Flowchart.....	50
Figure 7.2: Post-Lockdown Testing Schedule	51
Figure 7.3: Batteries Discharge Test	51
Figure 7.4: The Internal Resistance with the Consumed Current	52
Figure 7.5: Motor Static Test	52
Figure 7.6: The Test Connector.....	52
Figure 7.7: Test Setup	53
Figure 7.9: Landing Gear Test Setup	53
Figure 7.8: The Landing Gear Test Simulation	53
Figure 7.10: FEA of Motor Mount	54
Figure 7.11: FEA of Shipping Container	54
Figure 7.12: The Pre-flight Checklist	55
Figure 7.13: Aircraft Inspection Checklist	55
Figure 8.1: The Discharge Curve of 6 Cells LiPo Battery Pack (6000 mAh) at 34A	56
Figure 8.2: Predicted and Actual Static Thrust for M_2 and M_3	56
Figure 8.3: Predicted and Actual Dynamic Thrust for M_2 and M_3	57

List of Tables

Table 3.1: Analysis of Mission Requirements	12
Table 3.2: Desired Performance.....	13
Table 3.3: Figures of Merit.....	14
Table 3.4: Aircraft Configuration Selection	15
Table 3.5: Fuselage Design Selection.....	15
Table 3.6: Wing Placement Selection.....	16
Table 3.7: Propulsion System Configuration	16
Table 3.8: Tail Assembly Configuration.....	17
Table 3.9: Landing Gear Configuration	17
Table 3.10: Stabilizing Surfaces Configuration	18
Table 4.1: The Selected Design Point	22
Table 4.2: The Combinations Selected by the Code	23
Table 4.3: Preliminary Parasite Drag.....	26
Table 4.4: Parasite Drag Coefficient for $M2$	27
Table 4.5: Parasite Drag Coefficient for $M3$	27
Table 4.6: Aileron, Elevator and Rudder Sizing Parameters.....	29
Table 4.7: Aileron, Elevator, and Rudder Dimensions	29
Table 4.8: The Required Elevator Deflection	29
Table 4.9: Trim AoA for each Mission	30
Table 4.10: Acceptable Ranges for Each Mode	31
Table 4.11: Dynamic Stability Characteristics for Each Missions	32
Table 4.12: Calculated Performance of Each Mission	32
Table 5.1: Characteristic Parameters of the Final Aircraft.....	33
Table 5.2: Final Propulsion System for Each Mission	39
Table 5.3: Weight and Balance Table	40
Table 5.4: Estimated Performance of the Aircraft in Each Mission	41
Table 5.5: Missions Score Prediction	41
Table 6.1: Manufacturing Process FOM.....	46
Table 6.2: Manufacturing Process Investigation	47
Table 7.1: Testing Objectives	51

Acronyms, Abbreviations, and Symbols

UDC	Unmanned Aerial Vehicles Development Centre	$C_{L_{Cruise}}$	Cruis Lift Coefficient	δ_R	Rudder Deflection
DBF	Design/Build/Fly	v_{turn}	Turning Speed	W	Aircraft Weight
UAV	Unmanned Aerial Vehicle	v_{cruise}	Cruising Speed	P	Power
CFD	Computational Fluid Dynamics	S_{ref}	Reference Surface Area	P_{req}	Power Required
CAD	Computer Aided Design	FF	Form Factor	CG	Center of Gravity
FOM	Figure of Merits	Q	Interference Factor	SM	Static Margin
M1	Flight Mission 1	C_f	Skin Friction Coefficient	NP	Neutral Point
M2	Flight Mission 2	C_m	Moment Coefficient	MAC	Mean Aerodynamic Chord
M3	Flight Mission 3	AR	Aspect Ratio	Re	Reynold's Number
GM	Ground Mission	V_h	Horizontal Tail Volume	e	Oswald efficiency
$N_{containers}$	Number of Containers	S_h	Horizontal Tail Planform Area	AoA	Angle of Attack
T_{M2}	Mission 2 Time	V_v	Vertical Tail Volume	ζ	Damping Ratio
N_{laps}	Mission 3 Number of Laps	S	Wing Planform Area	ω_n	Undamped Natural Frequency
L_{Sensor}	Length of the Towed Sensor	b	Wing Span	ω_d	Damped Frequency
W_{sensor}	Weight of the Towed Sensor	S_a	Aileron Planform Area	τR	Time Constant
T_{GM}	Ground Mission Time	b_a	Aileron Span	t_2	Time to Double Amplitude
NiCad	Nickel Cadmium	C_a	Aileron Chord	$t_{\frac{1}{2}}$	Time to Half Amplitude
NiMh	Nickel Metal Hydride	b_{ai}	Aileron Inner Edge to the wing root distance	ESC	Electronic Speed Controller
LiPo	Lithium Polymer	δ_A	Aileron Deflection	C_{df}	Skin Friction Drag Coefficient
MTOW	Maximum Takeoff Weight	S_E	Elevator Planform Area	C_{fc}	Skin Friction Coefficient
D	Drag Force	b_E	Elevator Span	$S_{wet,body}$	Body Wetted Surface Area
L	Lift Force	C_E	Elevator Chord	$S_{wet,fins}$	Fins Wetted Surface Area
C_D	Drag Coefficient	δ_E	Elevator Deflection	A_{BT}	Body Tube Reference Area
C_L	Lift Coefficient	S_R	Rudder Planform Area	fb	Rocket Fineness Ratio
C_{D0}	Parasite Drag Coefficient	b_R	Rudder Span	c	Average Chord Length
$C_{L_{Max}}$	Maximum Lift Coefficient	C_R	Rudder Chord	t	Fin Thickness

1.0 Executive Summary

This report demonstrates the Cairo University UDC team's planned approach for the 2020-2021 AIAA DBF competition. This year's main objective –as illustrated by the AIAA guidelines– is to simulate a functional UAV with a towed-sensor suite for surveillance operations as well as reliable cargo transportation. The aircraft should be designed to sustain the full remote deployment, operation, and recovery of a towed sensor, while maintaining high aerodynamic stability and performance in the flight course. Furthermore, the UAV should be capable of completing the flight course with/without onboard sensors secured in containers.

1.1 Design Process

The missions along with the design constraints and scoring criteria were thoroughly studied in the process of ensuring the mission requirements fulfillment. Then, a sensitivity analysis was conducted to identify the impact of various parameters on the overall competition score and maximize it. It was found that the sensor length, apart from the design report score, is slightly more affecting on the score. However, it was also found that the most scoring aircraft is that which balances between the number of carried shipping containers and the towed sensor length.

Afterwards, the sensitivity analysis results along with the current team capabilities were utilized to estimate initial parameters for the aircraft in the beginning of the preliminary design. The initial estimations were used as inputs to a designed MATLAB framework aircraft sizing tool, and mission modeler for sizing the aircraft and calculating its respective score. Iterations were made over a range of data collected in a database of UAVs of the same scale to find the preliminary design that maximizes the overall score with maintaining the desired stability of the aircraft. Following, the sizing of each sub-system was finalized in the detailed design section. An iterative phase of manufacturing and testing then took place to ensure that the aircraft fulfills all requirements and meets the targeted performance.

1.2 Performance and Capabilities of the Design

The designed aircraft (Horrus II), shown in *figure 1.1*, is expected to be capable of successfully completing the delivery flight in 1.36 minutes, while carrying 4 shipping containers as the payload. In addition, Horrus II will tow a 27.56 *in* sensor that weighs 0.53 *lb* for 16 laps within the ten-minute flight window of the sensor flight. The aircraft's mechanism was tested and successfully showed smooth deployment and recovery of the towed sensor. The aircraft's capabilities and performance will be tested and verified through individual subsystem tests and flight tests.

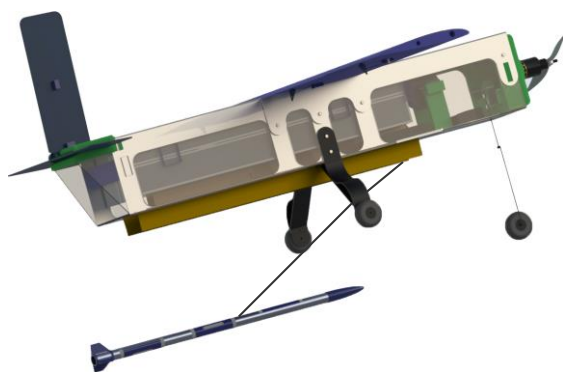


Figure 1.1: The Final Aircraft (Horrus II)

2.0 Management Summary

2.1 Team Organization

This year, the Cairo University UDC team includes 23 undergraduates: five seniors, six juniors and twelve sophomores, in addition to a post-graduate chief engineer and two faculty advisors. The new members are the sophomores, who were selected due to their skills and efforts which accentuated in the 2020 UDC local DBF. The rest of the team members have participated at least once in the previous AIAA DBF. This merge of the experience and creativity is the reason for the team development, and hence increasing the team's knowledge and rank along with its rank with each participation.

The Team is mainly divided into four sub-teams; Aerodynamics, structure, propulsion, and technical writing. The aerodynamics sub-team conducts the aircraft sizing, in addition to the stability and performance analysis. The design, manufacturing, and testing of the aircraft structures and mechanisms are carried out by the structure sub-team. Sizing, selection, and testing of the aircraft propulsion system are the responsibilities of the propulsion sub-team. The technical writing sub-team conducts a clear concise documentation for the several phases of the project.

A weekly meeting is held in which all the sub-team leaders report the individual sub-team progress over the past period, and all the members brainstorm and share opinions. The decision-making is based on the discussion and consultations among all the members, the leader, and the chief engineer, where any proposed idea is carefully evaluated to analyze its influence on the project.

2.2 Management Chart

Figure 2.1 outlines the team hierarchical structure and the role of each member in the UDC team. This structure defines the role of each member and organizes the communication between all members. The two faculty advisors are available for any necessary consultation regarding the project. The chief engineer supervises the progress of the team. The team leader is responsible for distributing the workload among the four sub-teams and ensures that all the project's needs are met within the budget limit. The four sub-team leaders assign the weekly tasks for each team member and report the team progress to the team leader. Lastly, any technical advice over the course of the project is offered by the six sub-team advisors for the individual sub-teams.

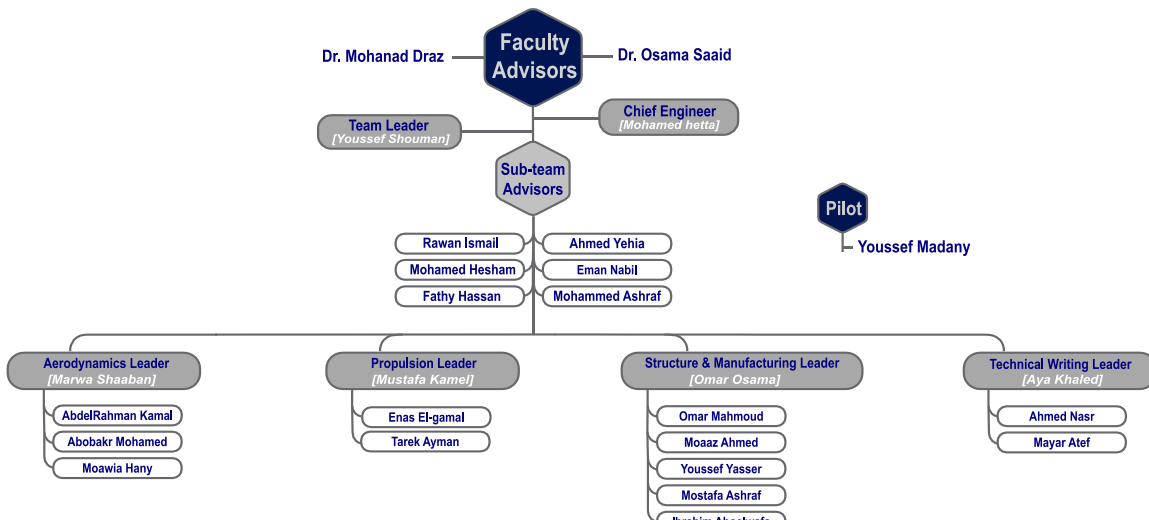


Figure 2.1: Team Structure

2.3 Milestone Chart

In order to ensure that the team is on track throughout the project, a Gantt chart was established at the beginning of the scheme to map out major milestones that needed to be met. The layout of the chart was essential to develop a competing design for a triumphant participation in the competition. The team leader oversaw the commitment to deadlines ensuring that all phases were completed as planned. The planned and actual schedules are shown in *figure 2.2*.

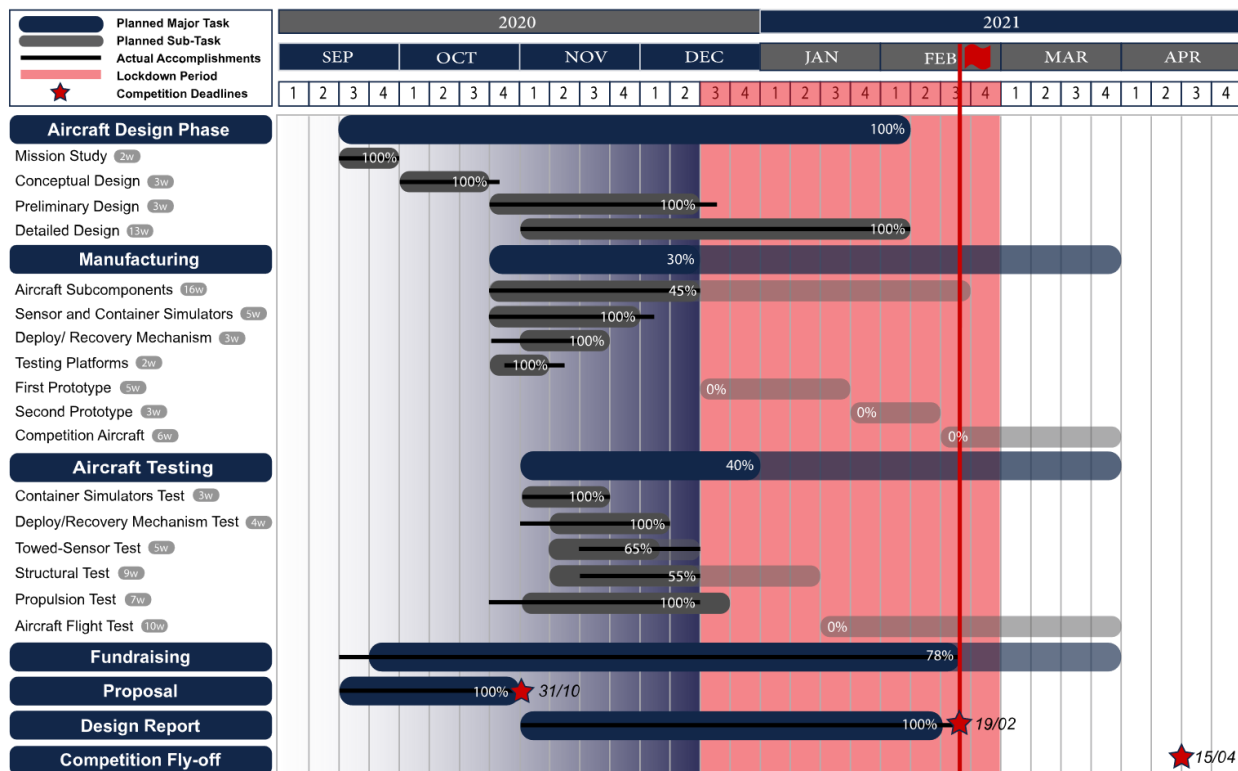


Figure 2.2: Milestone Gantt Chart

However, a lockdown started in mid-December and will be continued till the beginning of March. This lockdown postponed most of the manufacturing and testing processes. A new compact schedule had to be made to compensate the lockdown period to meet the virtual fly-off deadline. The new post-finals schedule is illustrated in *figure 2.3* below.

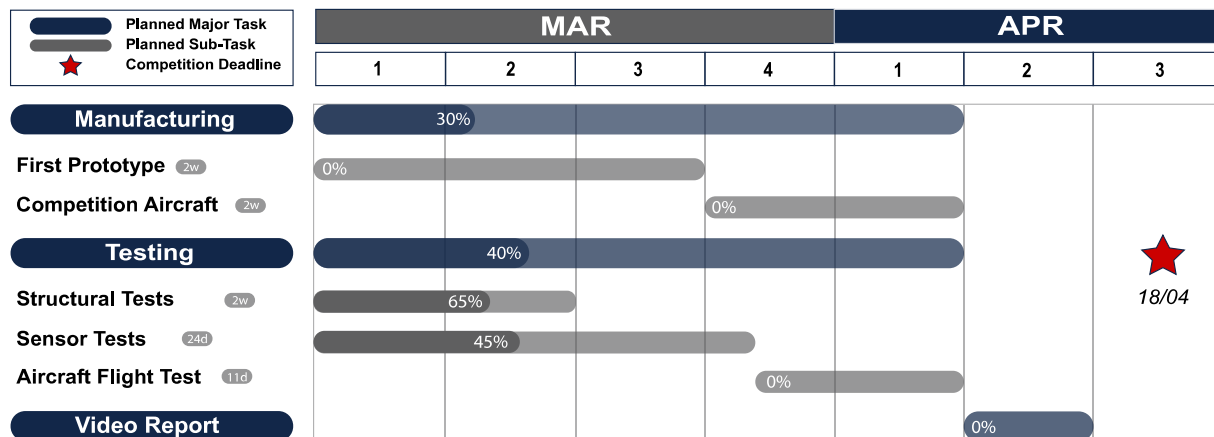


Figure 2.3: Post Lockdown Milestone

3.0 Conceptual Design

In this section, the competition requirements, as stated in the 2021 AIAA DBF rules, were studied and translated into design parameters. Afterwards, the scoring equations were analyzed to determine the design parameter which affects the score the most. Hence, several configurations were compared to select the highest scoring aircraft.

3.1 Mission Requirements

The 2020-2021 AIAA DBF competition's rules accentuate a towing-sensor aircraft. It must be capable of delivering the sensor conserved in its shipping container as well as shipping container simulators. The aircraft performance will be tested in the contest through three flight missions and one ground mission.

Prior to the takeoff, the payload must be installed in less than 5 minutes. The aircraft must take off within 100ft with the payload of each flight mission. The heaviest payload belongs to $M2$; it consists of the sensor conserved in its shipping container and the shipping container simulators besides the deploying and recovery mechanism. *Figure 3.1* shows the competition flight course in detail. This flight course tests the aircraft stability by performing straightaways, two 180°-turns, and a 360°-turn maneuver. In all flight missions, the time starts when the aircraft throttle is advanced and ends when it passes over the starting line in air; successful landing without bouncing off is necessary to get the mission score.

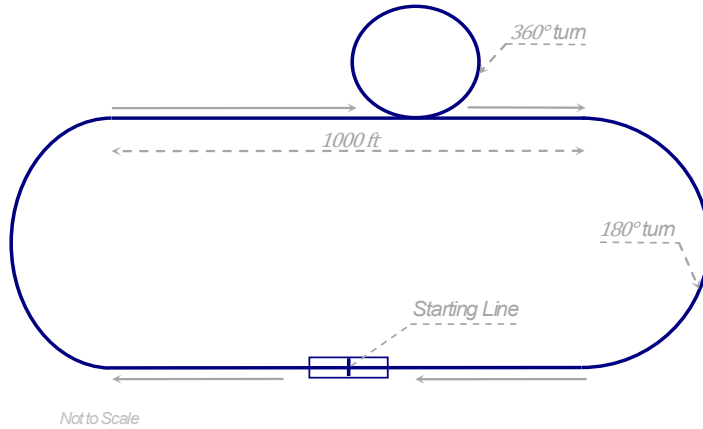


Figure 3.1: Course Layout

3.1.1 Missions and Scoring Summary

The overall score of each team is given by *equation (3.1)*

$$Score = Written\ Report\ Score \times Total\ Mission\ Score, \quad (3.1)$$

where the *Written Report Score* depends on the degree to which the design report presents the required information and adheres to the requirements. On the other hand, the *Total Mission Score*, given by *equation (3.2)*, depends on each mission score, which will be discussed in details in this section.

$$Total\ Mission\ Score = M1 + M2 + M3 + GM, \quad (3.2)$$

where $M1$, $M2$ and $M3$ stand for the three flight missions score, while GM represents the ground mission score.

- Flight Mission One – The Staging Flight

This mission tests the ability of the aircraft to fly without any payload. It requires the aircraft to complete 3 laps within a 5-minute flight window. If it is successful, the mission score will be $M_1 = 1$ otherwise $M_1 = 0$.

▪ Flight Mission Two – The Delivery Flight

This mission is similar to the Staging Flight mission, but the aircraft is loaded here. The payload is the sensor conserved in its container, the shipping container simulators as well as the deployment and recovery mechanism. The mission score is given by *equation (3.3)*

$$M2 = 1 + \left[\frac{\left(\frac{N_{containers}}{T_{M2}} \right)}{\left(\frac{N_{containers}}{T_{M2}} \right)_{Max}} \right], \quad (3.3)$$

where $\left(\frac{N_{containers}}{T_{M2}} \right)$ is the ratio of the number of the carried containers to the flight time of the team. The number of the carried containers is the sum of the shipping container simulators and the sensor container. $\left(\frac{N_{containers}}{T_{M2}} \right)_{Max}$ is the highest ratio of all teams.

▪ Flight Mission Three – The Sensor Flight

The aircraft with the towed sensor and the deployment and recovery mechanism must complete as many laps as possible within a 10-minute flight window. The sensor will be remotely deployed prior to the first 360-degree turn. After the final 360-degree turn, the sensor will be recovered remotely. However, the aircraft can't land before the fully recovery inside the aircraft. The score is given by *equation (3.4)*

$$M3 = 2 + \left[\frac{\left(N_{laps} \times L_{Sensor} \times W_{sensor} \right)}{\left(N_{laps} \times L_{Sensor} \times W_{sensor} \right)_{Max}} \right], \quad (3.4)$$

where $(N_{laps} \times L_{Sensor} \times W_{sensor})$ represents the number of laps performed by the team while towing a sensor with these dimensions, and $(N_{laps} \times L_{Sensor} \times W_{sensor})_{Max}$ represents the highest product of all teams.

▪ The Ground Mission – Operational Demonstration

This mission requires the demonstration of *M2* and *M3* on the ground to test the ease of the payload installation and the aircraft accessibility. It can be attempted at any time during the contest. It consists of two stages. A non-timed stage demonstrates the container's rigidity and functionality by dropping it on all six sides from a ten-inch height. The sensor enclosed inside it will, then, be checked for any physical damage. In addition, the sensor will be operated to demonstrate that it meets all functions required for *M3*. The other stage is a timed stage that includes two phases.

The first phase is the installation of *M2* full payload. Then, the time is stopped, and the pilot demonstrates that the flight controls are active. The second phase is the un-installation of *M2* payload and installation of *M3* payload. Then, the time is stopped, and the pilot demonstrates that the flight controls are active. Then, the assembly crew member holds the aircraft, and the pilot demonstrates the sensor deploying and recovery mechanism. Throughout the mission, the time is calculated when the assembly crew member crosses the start/finish line. The mission score is calculated by *equation (3.5)*

$$GM = \frac{(T_{GM})_{min}}{T_{GM}}, \quad (3.5)$$

where T_{GM} is the time taken by the team to accomplish the mission, and $(T_{GM})_{min}$ is the least time for all teams.

3.1.2 Aircraft General Constraints

Beside the mission requirements, general constraints were specified by the rules:

Configuration

- All payloads must be internally conserved; no external surfaces or features are allowed.
- The wingspan must not exceed 5 *ft*.

Takeoff and Landing

- A runway must be used for taking off and landing; hand-launching is not allowed.
- The takeoff limit is 100 *ft*.

Propulsion

- The allowed batteries types are NiCad/NiMH or Lithium Polymer (LiPo) batteries; moreover, the propulsion batteries must be of the same type.
- The maximum allowable total stored energy for the propulsion system is 200 *Wh*.
- In case of using NiCad/NiMH batteries, they can be either individual battery cells or commercially-procured battery pack.
- In case of using LiPo batteries:
 - in case of implementing more than one battery pack for a single purpose, all commercially battery packs must be identical and parallel-connected to each other.
 - They must be commercially-procured and unaltered battery pack.
 - at least, a 0.25 *in* of air gap is required between each two packs.
- Each pack cannot exceed 100 *Wh*.

Payloads

- The sensor
 - It is cylindrical; its minimum dimensions are one-inch in diameter with a four-length-to-diameter ratio.
 - It must remain in a fixed orientation during flight.
 - It must have three external lights visible in lots of sunshine which operates remotely in a certain pattern.
 - It must have its own battery power supply along with a physical connection to the airplane.
 - The towing cable length must be ten times the sensor length, starting from the exit location in the aircraft.
 - Must have a fixed configuration; no parts can be folded/unfolded during deployment.
- The shipping container
 - The shipping container must enclose and protect the sensor from damage during the drop test.
 - The shipping container simulators must have the same weight (or greater) of the sensor in its container.
 - The size of the shipping container simulators must have the same dimensions of the sensor container with a clearance of $\pm \frac{1}{8}$ *in*.

3.2 Design Requirements

2020-2021 DBF competition scoring equations and guidelines were carefully analyzed to conduct the design process. The analysis results influenced the decision-making process for maximizing the total score; thus, a design approach was adopted in addition to the aircraft configuration selection. Design requirements were defined for each score section and are tabulated in *table 3.1*.

Table 3.1: Analysis of Mission Requirements

Missions		Mission Requirements	Design Parameters
Ground Mission		<ul style="list-style-type: none"> • Fast loading and unloading of the shipping container simulators • Rigid Shipping container • Reliable deploy/recovery mechanism 	T_{GM}
Flight Missions	Mission 2	<ul style="list-style-type: none"> • Balancing the three laps time and the number of the shipping container simulators 	$\frac{N_{containers}}{T_{M2}}$
	Mission 3	<ul style="list-style-type: none"> • Balancing the towed sensor length and weight with the number of laps flown within the flight window 	$N_{Laps} \times L_{Sensor} \times W_{Sensor}$

3.2.1 Score Sensitivity Analysis

Initial Investigation of the scoring equations demonstrated that there are two principal design parameters: the number of carried shipping containers and the length of the towed sensor. All Other design parameters, mentioned in *table 3.1*, are dependent and were related to the main design parameters. It was also noted that maximizing the number and length of the sensors will increase both the payload weight and the drag on the towed sensor in flight. However, this was favored over maximizing the cruise speed due to the $200Wh$ propulsion power total stored energy constraint.

The team developed a MATLAB sizing framework to evaluate the effect of varying those parameters on the overall score and obtain the most scoring aircraft in the fewest number of iterations possible. This is implemented by an optimization loop where the number of carried shipping containers and towed sensor length, battery cells and capacity for each mission are varied. Constrained by the missions' payload specifications and energy requirements enforced by the rules, the framework calculates the fuselage dimensions, selects the best airfoil fit from a large database and sizes the control surfaces and high lift devices if needed. Afterwards, stability analysis is conducted followed by drag and power calculations and hence the propulsion group sizing. Once the aircraft is sized, the score of each combination of the optimization factors is calculated for $M2$ and $M3$. T_{GM} is then calculated using an empirical equation; function of the carried shipping containers number.

The overall score was then calculated and plotted to find the best combination. *Figure 3.2* shows the corresponding towed sensor length, time of the delivery mission, number of laps in the sensor flight mission, total score and the number of carried shipping containers indicated by the size of circles. The analysis showed that the most scoring aircraft, indicated by the yellow circle, carries 6 shipping containers, each weighting 0.53 lb . within 1.54 min in $M2$, and performs 20 laps while towing a 31.5 in. sensor in $M3$.

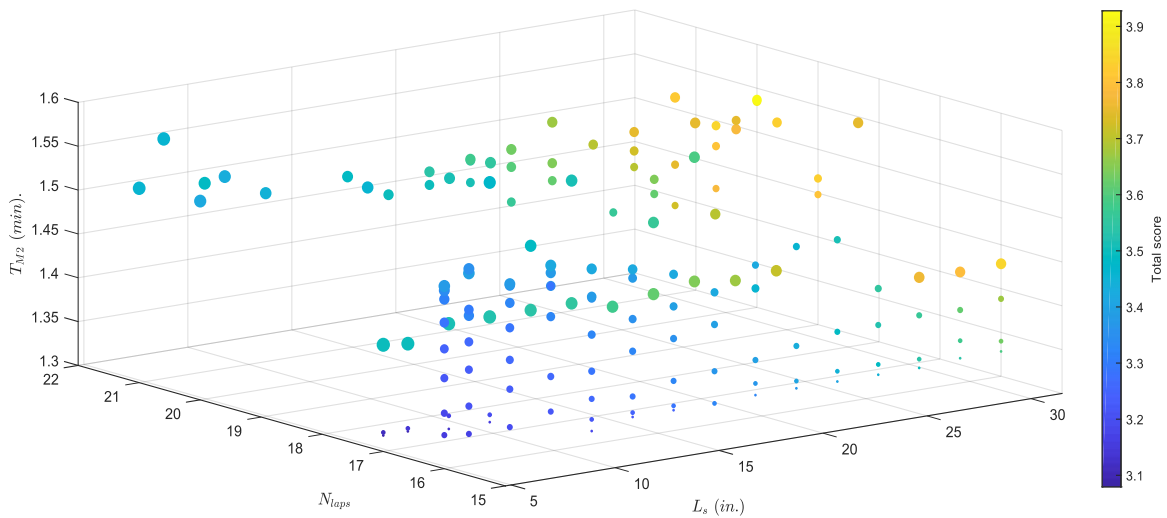


Figure 3.2: Estimated Score of Various Design Scenarios

3.2.2 The Translation into Design Requirements

Considering the score analysis results as well as the team's previous performance, the aircraft performance was targeted as shown in *table 3.2*.

Table 3.2: Desired Performance

Parameter	$N_{containers}$	T_{M2}	L_{Sensor}	N_{Laps}	W_{Sensor}	Estimated Score
Value	4	81.6 sec	27.56 in	16	0.53 lb	3.83

After the analysis of missions' aspects and the scoring scheme, the main design requirements were derived, which will be used in the coming section as the key points of configuration down-selection through the Figures of Merit (FOM) method. Those requirements are listed below.

- **Payload Capacity:** In order to maximize the score of $M2$, the aircraft's empty weight should be as light as possible –without affecting the structural integrity; thus, allowing for more shipping containers to be carried; consequently, lighter configurations are favored.
- **Stability:** The length of the sensor is a leading factor contributing to $M3$ score, hence; increasing the sensor's length would increase $M3$ score. Accordingly, the aircraft must be stable enough to withstand the deploying impact and disturbances induced by the towed sensor.
- **Speed:** The aircraft score in $M3$ depends on how many laps the aircraft will finish within 10 minutes–while carrying the deployed sensor– and therefore, the chosen configuration should satisfy this requirement in order to be considered. Configurations that are characterized by high drag will not be contentious.
- **Mechanical Reliability:** Reliability of the sensor's container as well as the deployment and recovery mechanism are vital, where the ground mission will demonstrate the capability of the shipping container to protect the sensor; moreover, the ground mission is a time mission in which the time it takes to demonstrate the mechanism will be counted, which requires the mechanism to be simple and easy to operate.

3.3 Configuration Selection

Following the mission study phase, various conceptual designs were proposed by the team members; each design was superior with specific aspects that distinguish it from the rest. In order to organize the selection phase, the design parameters, defined in *section 3.2*, were translated into three figures of merit, FOMs. Each FOM is derived from either a single or multiple design parameters. Moreover, a fourth design-parameter-independent FOM, manufacturability, was added to account for the ease of multiple prototyping which offers further testing for a reliable final aircraft. Score factors state, quantitatively, the impact of the respective design parameters on the overall score, based on the sensitivity analysis, demonstrated in *section 3.2*. Hence, each FOM was assigned a score factor, varying from one to four, that indicates its significance; a score of one means it is the least significant factor, while a score of four means it is the most significant one. Each FOM with its corresponding design parameters and score factor is shown in *table 3.3* below.

Table 3.3: Figures of Merit

Figure of Merit	Parameter Affected	Score Factor
High Payload Capacity	$N_{Containers}, W_{Sensor}$	4
Low Drag	T_{M2}, N_{Laps}	3
Light Weight	All the parameters	2
Manufacturability	—	1

In selecting each component or design feature of the aircraft or the payload, those figures of merit were utilized to compare and assess the candidates for that component or feature. Other FOMs that are related directly to each individual component or feature are included along with the four main FOMs for a thorough assessment. This includes selecting the overall aircraft configuration, the fuselage configuration, the wing placement, the propulsion system, the empennage configuration, and the sensor stabilizing surfaces that best meet the design requirements and maximize the overall score.

Individual candidates for each design feature were given a mark from one to three; that mark identifies the extent to which the candidate achieves that FOM relative to the other candidates. The score of each candidate is its mark multiplied by the corresponding score factor; the candidate with the highest total score is, hence, chosen.

3.3.1 Overall Aircraft Configuration Selection

Table 3.4 demonstrates the selection approach for the overall aircraft configuration, through the FOM mean. Two candidates were chosen for the overall aircraft configuration: conventional and flying wing. As shown in the FOM table below, the conventional aircraft would fly with a lower speed relative to its counterpart, hence increased time in $M2$ and fewer laps in $M3$. The conventional configuration, however, offers the maximum storage capacity, which maximizes the number of carried sensor shipping container simulators in $M2$ and the length of the individual sensor that must be secured inside the aircraft volume. In addition, the conventional aircraft is more stable, which will help in compensating the destabilizing effect of the towed sensor. Therefore, the conventional configuration achieves the highest total score and was accordingly chosen.

Table 3.4: Aircraft Configuration Selection

			
Figure of Merit	Factor	Conventional	Flying Wing
High Payload Capacity	4	3	1
Low Drag	3	3	2
Light weight	2	2	3
Stability and Control	1	3	1
Manufacturability	1	3	2
Total Score		31	19

3.3.2 Fuselage Configuration Selection

Two candidates were chosen for the fuselage configuration: round edged and lifting body. From the data previously collected from CFD analysis, the drag of the round edged fuselage body is still lower than that of the lifting body fuselage. This is mainly because to accommodate a reasonable number of the sharp-edged-payload a relatively huge lifting body would be chosen, and it would generate a significant lift with massive drag accompanied. In addition, as shown in *table 3.5*, the lifting body payload capacity is inferior relative to its counterpart, unless the fuselage was extremely maximized. The round-edged body scored higher for the high payload capacity as the payload is box-shaped. Furthermore, the round-edged fuselage is simpler and can be easily manufactured. So, the round-edged was chosen for this year's aircraft.

Table 3.5: Fuselage Design Selection

			
Figure of Merit	Factor	Round Edged	Lifting body
High Payload Capacity	4	3	1
Low Drag	3	2	1
Light weight	2	2	3
Manufacturability	1	2	1
Total Score		24	14

3.3.3 Wing Placement Selection

For this year's aircraft, three options were proposed for the wing placement: high wing, mid wing, low wing. As shown in the FOM *table 3.6* below, the mid wing would consume part of the internal volume (narrowing down the payload carrying capacity) as the wing spars would be passing through the middle of the fuselage body; hence, it's inferior when it comes to the most significant FOM, and it offers moderate performance for the rest of the FOMs. So, it was accordingly excluded. The high and low wing placements were each very competitive for this year's aircraft. The high wing placement, however, scores higher when it comes to stability. It is also the best choice since it has been decided that the sensor will be deployed and recovered from the fuselage floor. Hence, the high wing placement was chosen.

Table 3.6: Wing Placement Selection

Figure of Merit	Factor	High Wing	Mid Wing	Low Wing
		30	21	28
High Payload Capacity	4	3	1	3
Low Drag	3	2	3	2
Light weight	2	3	2	3
Stability and Control	1	3	2	1
Manufacturability	1	3	2	3
Total Sum Score		30	21	28

3.3.4 Propulsion System Selection

Table 3.7 shows the assessment of the proposed configurations for the propulsion system: single pusher, single tractor, and double tractor. As shown in the FOM table below, double tractors have the highest payload capacity since the motors are mounted on the wings, where they do not consume much of the internal payload storage volume. They offer, however, moderate performance in the rest of the FOMs along with having the highest overall system weight. In addition, double tractors are generally less efficient due to the increased combined losses from the two motors. Single tractors, on the contrary, have the lightest overall system weight, while the single pushers have the least drag. The single tractors, nevertheless, have a better propeller efficiency as the air that passes by the propeller is undisturbed; hence, single tractors offer higher speed with high payload capacity onboard, because the thrust generated increases with the efficiency.

Furthermore, choosing single pushers compromises the towed sensor stability, which is a top priority, as this might interfere with the sensor while performing turns and maneuvers or by just disturbing the air flow behind the aircraft; hence, it scored the least in the positive impact on the sensor performance. Therefore, single tractors were deemed the best option in the propulsion system for this year's aircraft.

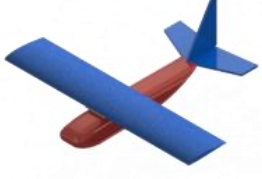
Table 3.7: Propulsion System Configuration

Figure of Merit	Factor	Single Pusher	Single Tractor	Double Tractor
		20	26	21
High Payload Capacity	4	2	2	3
Low Drag	3	3	2	1
Light Weight	2	2	3	1
Positive Impact on Sensor Performance	1	1	3	3
Manufacturability	1	2	3	1
Total Score		20	26	21

3.3.5 Empennage Configuration Selection

Conventional tail and T-tail were possible options for the empennage configuration. There are mild differences between the two, and, as shown in *table 3.8* below, their score is very close. Even though the T-tail is known for having an effective horizontal tail, due to its high position in a relatively undisturbed air flow, it has been rolled out as it would require a heavy structure to add integrity to the tail. The conventional tail configuration offered acceptable performance in all aspects and suited all this year missions along with being easy to be manufactured and integrated to the aircraft.

Table 3.8: Tail Assembly Configuration

			
Figure of Merit	Factor	Conventional	T-Tail
High Payload Capacity	4	3	3
Low Drag	3	2	2
Light weight	2	2	1
Stability and Control	1	3	3
Manufacturability	1	3	2
Total Sum Score		28	25

3.3.6 Landing Gears Selection

Options for the landing gear configuration included the tail dragger and the tricycle configurations. Since the configuration has no impact on the payload capacity, this FOM was replaced by the controllability. The tricycle configuration was chosen due to its lightweight, manufacturing simplicity, and controllability, as shown in *table 3.9*.

Table 3.9: Landing Gear Configuration

			
Figure of Merit	Factor	Taildragger	Tricycle
Controllability	4	1	2
Low Drag	3	2	1
Light Weight	2	1	2
Manufacturability	1	1	2
Total Score		13	17

3.3.7 Sensor Stabilizing Surface Selection

To ensure that the sensor will be aerodynamically stable, multiple stabilizing approaches were investigated. The best chosen two are shown and compared in *table 3.10* below. As can be seen, the planar fins were superior in every aspect except for a slight difference in the overall weight for the same performance. The weight difference, however, was not impactful enough. Hence, planar fins were chosen for stabilizing the sensor.

Table 3.10: Stabilizing Surfaces Configuration

Figure of Merit	Factor	Planar Fins	Shuttle cock
High Payload Capacity	4	2	1
Low Drag	3	2	1
Light weight	2	1	2
Stability and Control	3	2	1
Manufacturability	1	2	1
Total Sum Score		24	15

3.3.8 Sensor Configuration

The sensor design must be reliable, while integrating between its length and strength. Two sensor designs were considered by the structure sub-team. The entire structure of the first configuration was composed of metallic spars and 3D-printed parts, as can be shown in *figure 3.4*. Earlier, it was a combination of metal spars alongside wooden spars and rings. Sensor testing, however, showed that wood was not reliable for a 27.56 in. sensor, and it was excluded from the design. All wooden parts, however, have been replaced by 3D-printed rings and metallic spars. A hollow-metallic cylindrical sensor is the second configuration, featuring 3D-printed parts as the LEDs housing units. Using double face tape, the base is connected to the cylinder, while the cover is the housing unit of the batteries. The second configuration, shown in *figure 3.4*, had the advantage of being easier to manufacture and is much lighter; hence, it was chosen.

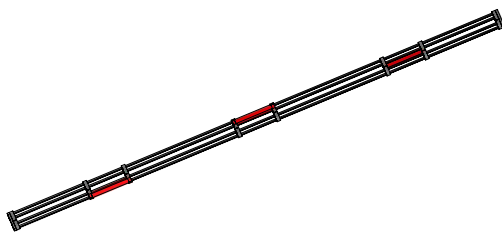


Figure 3.4: The First Sensor Configuration



Figure 3.4: The Second Sensor Configuration

3.3.9 Deployment/Recovery Mechanism Selection

The mechanism must deploy and recover the sensor during flight course to fulfill *M3*, it should be reliable, easy to recover, and light in weight. The structure sub-team has proposed two main configurations for the sensor mechanism. In the first configuration, the sensor will be deployed and recovered to the container through two doors in the bottom of the fuselage attached to two legs that are connected to each other by a joint connected to a servo as shown in *figure 3.6*.

The other configuration conceptualized a sensor that is held in an inclined position with its container – to facilitate its release, and the sensor is pushed against a spring inside the container. The door is closed while a ratchet wheel is locked to ensure the sensor remains in its place until the order of release. However, this configuration failed the design requirements; the spring was very hard and not suitable for the mechanism scale.

Besides, the sensor was held from its tip, causing the sensor to be stuck at the doorway unable to find its way back inside the container during recovery. Additionally, the more the inclination, the easier it becomes to release and recover the sensor; however, the higher the inclination angles are, the more consumed space inside the fuselage is. The second mechanism is shown in *figure 3.6*.

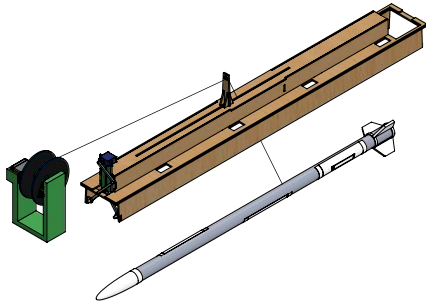


Figure 3.6: First Mechanism

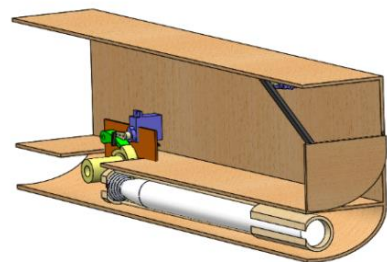


Figure 3.6: Second Mechanism

The first configuration had several advantages; it showed its effectiveness during recovery tests as it held the sensor from its CG, as well as its lightweight since it has fewer components.

3.4 Final Conceptual Design

After choosing the configuration of each sub-system, the final configuration selected, shown in *figure 3.7*, is a high wing, round-edged fuselage, single tractor with a conventional tail configuration. In addition, the tricycle landing gear was chosen as it enhances stability and eases the maneuvering. This configuration is designed to tow a 27.56 in. sensor in addition to carrying 4 shipping container simulators inside its fuselage.

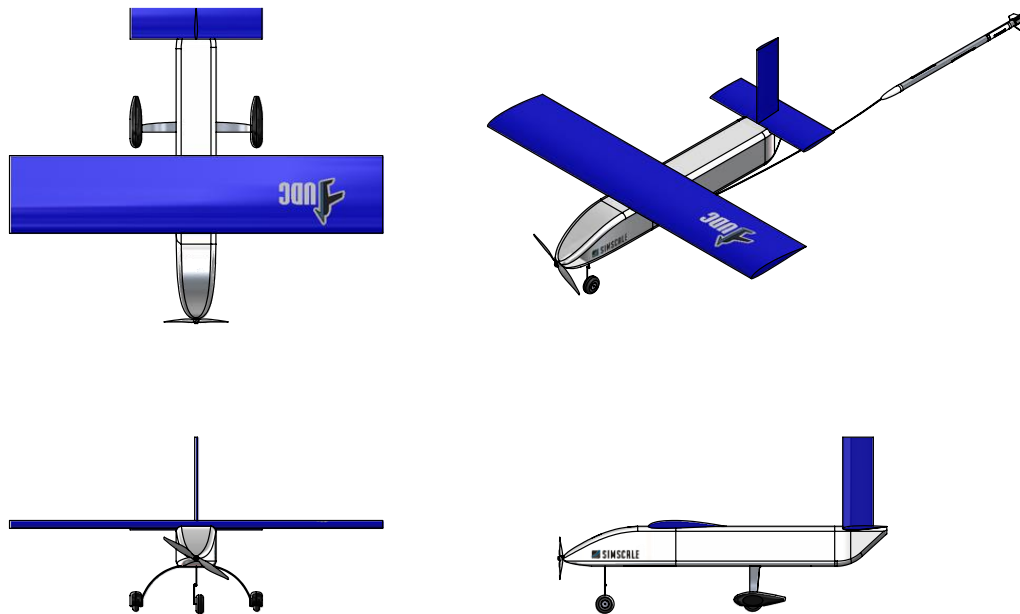


Figure 3.7: Final Conceptual Design

4.0 Preliminary Design

The purpose of the preliminary design was to optimize the aircraft's geometry and performance parameters in furtherance of maximizing the final score. The optimization was conducted through utilizing MATLAB based code that computes the aircraft's geometry and performance parameters, taking into account the trade studies, aerodynamics, mission modeling, and score analysis.

4.1 Design Methodology

The iteration process towards achieving the highest final score was used in specifying the parameters of the aircraft. Throughout the iteration process, the sensors' length, the number of sensors, the number of cells, and battery capacity were estimated. The design constraints set by the competition rules were taken into consideration to avoid unacceptable parameters. The block diagram, shown in *figure 4.1*, illustrates the methodology the code was based on.

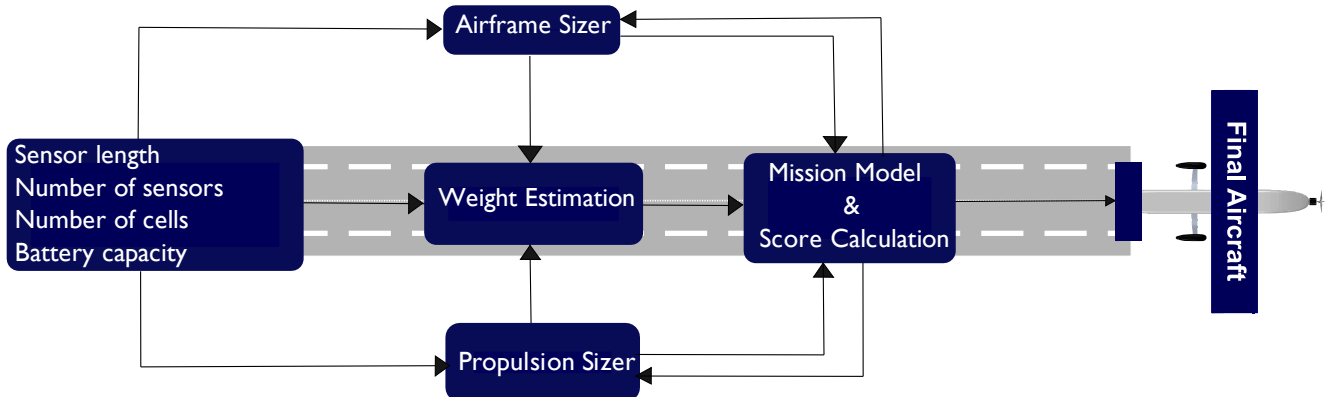


Figure 4.1: Flow Chart of the Team Design Methodology

Using the MATLAB code, a range was set for each parameter. The combination of all parameters was carried out in one stage. Within the given range, the code tests different combinations. Subsequently, the code takes each combination and determines all other airframe and propulsion parameters –Wing Area, airfoil, engine, propeller, etc.– corresponding to it. The next step in the code is to model the missions for each generated aircraft and compute the projected score. The aircraft delivering the highest score is the one to be used to specify the aircraft's parameters. It was decided that the optimal aircraft configuration was the one that balances between both $M2$ and $M3$.

4.2 Mission Model

4.2.1 Description and Capabilities

A mathematical model was constructed in order to closely determine and simulate the performance of the aircraft in the preliminary design process as well as the time needed for each mission. Thus, the flight course was separated into the following segments: take-off, climb, cruise, and turn, shown in *figure 4.2*. Each segment was modeled using equations from chapter 6 (Elements of Airplane Performance) in [1].

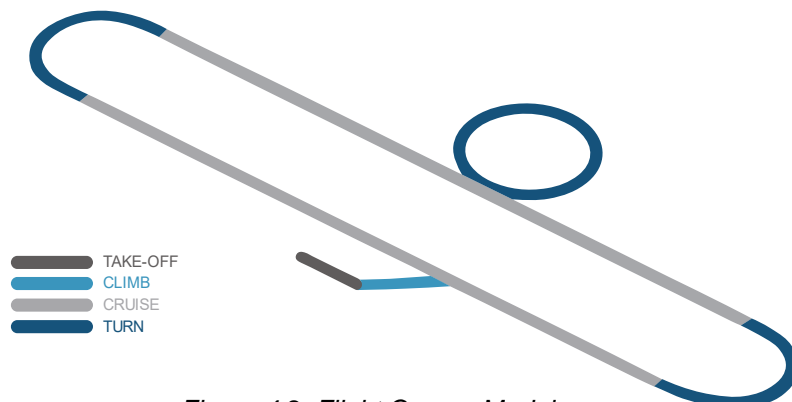


Figure 4.2: Flight Course Model

Takeoff was modeled by solving equation (4.1). It was assumed that the velocity when the aircraft leaves the ground is larger than the stall velocity.

$$v(t) = \sqrt{\frac{2ma}{\rho A C_d}} \tanh \left(t \sqrt{\frac{1\rho C_d A}{2m}} \right) \quad (4.1)$$

The following nonlinear equations (4.2), (4.3) were used to model the cruise flight condition.

$$m \cdot g - \frac{1}{2} \rho A C_l v^2 = 0 \quad (4.2)$$

$$T(v) - \frac{1}{2} \rho A C_d (C_l, v) v^2 = 0 \quad (4.3)$$

In order to simplify the model, it was assumed that turning occurs at maximum lift. The following equations (4.4), (4.5) yield the turning speed and radius.

$$T(v_{turn}) - \frac{1}{2} \rho A C_{d,max} v_{turn}^2 = 0 \quad (4.4)$$

$$R = \frac{2 \cdot m}{\rho \cdot A \cdot C_{l,max} \cdot \sin \alpha} \quad (4.5)$$

Moreover, the following equations (4.6), (4.7) were used to calculate the laps time.

$$t_{lap}(P, AR, m, A, C_l) = \frac{2 \cdot I}{v_0(P, m, A, AR)} + \frac{4 \cdot \pi \cdot R(P, m, n, C_{l,max}, AR)}{v} + 2 \quad (4.6)$$

$$t_{lap,first}(P, AR, m, A, C_l) = \frac{2 \cdot I - I_{takeoff}}{v_0(P, m, A, AR)} + \frac{4 \cdot \pi \cdot R(P, m, n, C_{l,max}, AR)}{v_{turn}} + 2 + t_{takeoff} \quad (4.7)$$

4.2.2 Uncertainties

As a result of several influences that cannot be fully controlled throughout the mission, there are some drawbacks and uncertainties to the preceding model. Below, significant uncertainties are described:

- **Wind:** in the above model, wind conditions were not considered, which may contribute to altitude loss due to head and crosswinds; however, the headwind tends to be 12.76 ft/sec on average upon checking the wind behavior during April month at Tucson, AZ.
- **Propulsion System:** the efficiency of the motor and propeller was assumed to be constant, which is not practical. The model does not allow for any variations in temperature that may influence the internal resistance of the batteries. The performance and durability of the propulsion system, however, are strongly dependent on wind conditions, altitude, and temperature. Consequently, based on these conditions, the thrust and drag equations may differ.
- **Human Error:** it was assumed that the pilot can operate the aircraft in its ideal conditions throughout the phases of the flight, including landing at slightly high speeds without slip, which is not reliable.
- **Sensor:** throughout the mission course, the sensor's response cannot be completely predicted. It is also uncertain that, particularly during turns, the sensor will sustain its stability. Besides, during deployment or release, there is a minor possibility that the sensor will be stuck at the mechanism's door.

4.3 Design Trades

4.3.1 Constraints Sizing

The aircraft should have a high cruising speed and MTOW to maximize the overall score. To achieve the MTOW, the stall speed and the lift coefficient ($C_{L_{Max}}$) should be maximized according to *equation (4.8)*. However, the higher the takeoff weight is the less the cruising speed is. Therefore, the optimal design is the one that balances between the cruise speed and the MTOW.

$$MTOW = L = 0.5 \rho V^2 S C_{L_{Max}} \quad (4.8)$$

A MATLAB framework is used to select the best aircraft geometry. The code objective is to estimate the weight of the aircraft as well as determine the dimensions of the fuselage, the wing and the tail empennage within the acceptable ranges. The output data was used to construct table 4.1 in addition to the matching plot, shown in *figure 4.3* where our design point was indicated.

Table 4.1: The Selected Design Point

Parameter	Wing Loading [W/S]	Power-to-Weight Ratio [P/W]	Wing Area [S]	Power Required [P_{req}]
Value	4.51 psf	62.22 $Watts/lb$	4.83 ft^2	1355.23 $Watts$

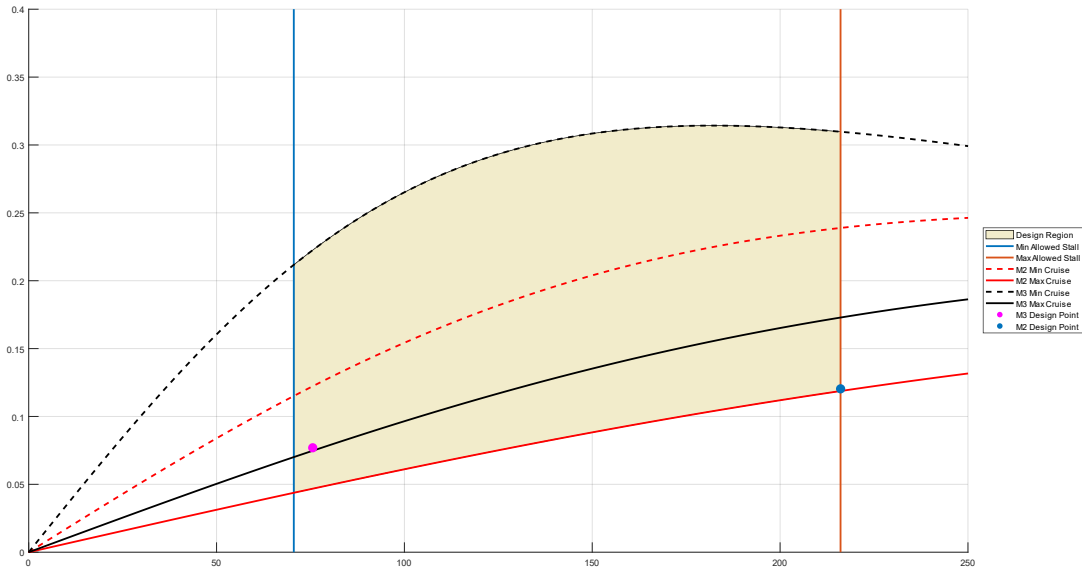


Figure 4.3: Matching Plot

4.3.2 Propulsion System Selection

As discussed in *subsection 3.2.2*, the high cruising speed and light empty weight are considered as main design parameters for this year's competition. This, in turn, was the criteria for the propulsion system selection, where the motor and battery combination offering the maximum dynamic thrust with the lightest weight. Hence, the Lithium Polymer (LiPo) batteries were preferred to the Nickel Metal Hydride (NiMH) and Nickel-Cadmium (NiCad) batteries. Since their energy density, specific energy, and C-rating are higher than those of the NiMH and NiCad batteries. Besides, the estimated weight of *M2* payload was greater than that of *M3*. Therefore, the propulsion system was designed to provide thrust in *M2* more than that of *M3*.

The design process was an iterative process conducted through a MATLAB framework. A database was constructed for each component in the system as code inputs, based on our previous experience and the available components in the UDC lab. The code, then, formed 200,000 combinations and calculated their performance parameters. Afterwards, they were filtered according to many criteria: the static and dynamic thrust, the RPM, the speed, the time of M_2 and M_3 , as well as the 200 watt-hour power limit for the entire system.

All systems which can perform all the required missions successfully passed the filtration stage. However, the code output was the three systems which have the highest power-to-weight ratios. *Table 4.2* illustrates the three propulsion systems selected by the code. The combination in the first row was favored in order to decrease the empty weight of the aircraft.

Table 4.2: The Combinations Selected by the Code

Motor	Battery Cells		Propeller		Static thrust (lb)		Motor Weight (lb)
	M_2	M_3	M_2	M_3	M_2	M_3	
Scorpion SII-4035-380kv	9 cells 3000 mAh	6 cells 6000 mAh	APC 17x8 E	APC 14x8.5 E	21.22	8.84	0.959
Scorpion HKIV-4035-330 (330)			APC 17x8 E	APC 14x8.5 E	19.29	6.84	1.005
KDE-Direct KDE700XF-295-G3			APC 17x8 E	APC 16x8.5 E	26.06	8.42	1.444

4.4 Aerodynamic Characteristics

In response to this year's guidelines for the DBF competition, the aerodynamics sub-team was focused primarily on two goals:

- **maximizing the lift-to-drag ratio**, ensuring a balance between the payload the aircraft is capable of accommodating, which directly affects M_2 score, and the speed by which it cruises, which directly affects M_2 and M_3 score. Moreover, this typically minimizes the thrust required for both M_2 and M_3 .
- **minimizing the parasite drag** on the towed sensor with its chosen stabilizing surfaces.

This, in turn, is an inevitable output for the designed MATLAB framework, discussed earlier in *section 4.1*. Hence, choosing the suitable airfoil and calculating the drag polar for the aircraft are both outputs of the code iterations. In addition, FlightStream CFD simulation was utilized to verify the drag polar of the aircraft due to the uncertainty of the build-up drag method which is the one used by the MATLAB framework.

4.4.1 Airfoil Selection

Researching UAVs and commonly used families of airfoils for that scale yielded numerous candidates for this year's aircraft. Hence, airfoils of interest were analyzed at 300,000 Reynold's number and the results were collected into a database of airfoils on which the code iterations would operate. It is, also, worth noting that airfoils with complex geometry that are beyond our manufacturing capabilities were excluded from the database.

The MATLAB framework filters the airfoils using two criteria: a maximum-thickness-to-chord ratio that accommodates a 0.5-inch-diameter wing spar, and a C_L , at a trimming angle interval $[0,4]^\circ$, that is equal to or higher than the desired cruising C_L for M_2 and M_3 that fulfills a desired cruising speed of about 98.4 ft/s . Airfoils that do not meet the chosen criteria are filtered out.

Afterwards, the selection criteria for the remaining airfoils were based on their C_{Lmax} and $(\frac{CL}{CD})_{max}$. This typically outputs two airfoils: the one with the highest C_{Lmax} among the list and the one with the highest $(\frac{CL}{CD})_{max}$ among the list. Both airfoils are then used in parallel for the rest of the code iterations reaching the mission model and the aircraft with the best score will settle it for the best airfoil among the two.

Iterating twice yielded s3002 airfoil, shown in *figure 4.4*, as the airfoil with both the highest C_{Lmax} and $(\frac{CL}{CD})_{max}$. Hence, it was chosen. With a C_{Lmax} of 1.5422 at a 15° AoA and a $(\frac{CL}{CD})_{max}$ of 86.69468 at a 5° AoA, the s3002 airfoil fulfills the desired performance for this year's aircraft. *Figure 4.5* demonstrates the selected airfoil performance analysis.

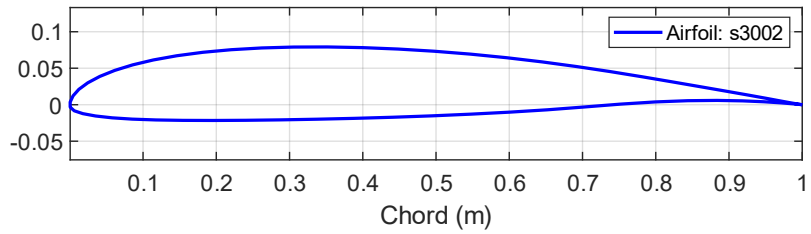


Figure 4.4: The Selected Airfoil

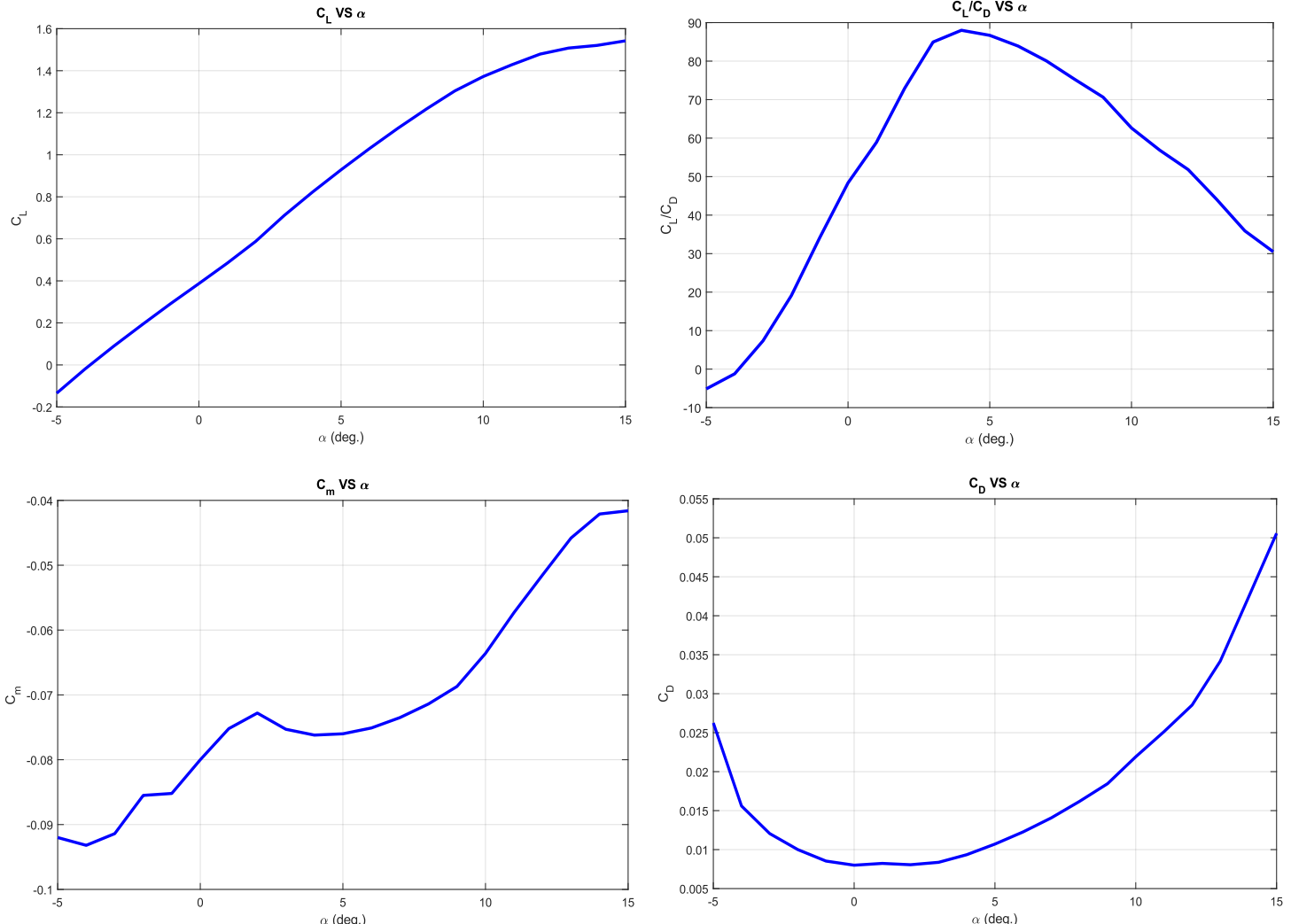


Figure 4.5: s3002 Performance

4.4.2 High-Lift Devices

It was determined that a $C_{L_{max}}$ of 1.8 is desired to accommodate the 4 sensors in $M2$, and compensating for the difference between the desired $C_{L_{max}}$ and the $C_{L_{max}}$ offered by the chosen airfoil, if there is any, was preferred by the team to be through utilizing a high-lift device that provides the remaining lift required to accomplish the mission. This was chosen instead of including highly cambered airfoils in the database, because even though they would provide the needed $C_{L_{max}}$, they would produce much higher drag at high speeds.

The framework, hence, deemed a plain flap necessary to increase the lift coefficient by 22%. The flap sizing was, also computed through code iterations for the dimensions that provides the desired lift. Hence, a plain flap with 0.3292 m span and 0.0898 m chord was chosen. *Figure 4.6* below demonstrates effect of extending the flaps by 30% with 25° on lift coefficient as a function of the AoA.

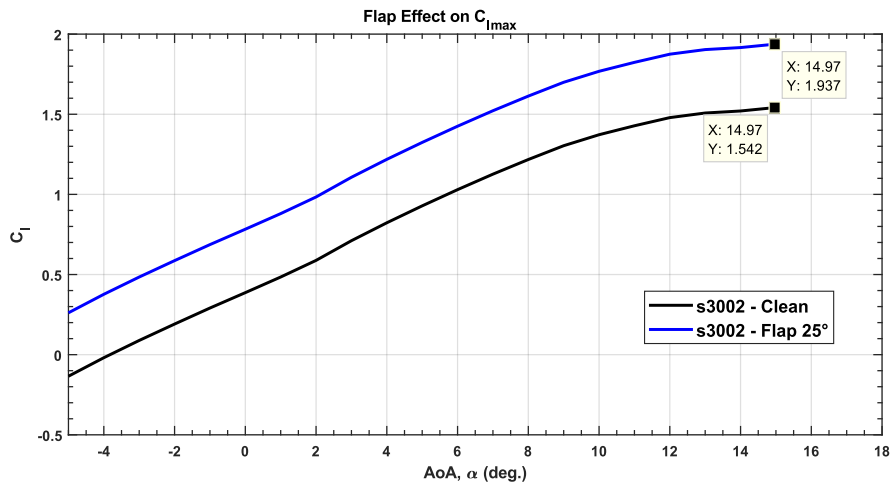


Figure 4.6: Flap Effect on the Lift Coefficient

4.4.3 Drag Calculation

Since drag calculation is crucial in estimating the aircraft performance and improving it, it was computed using two methods: through the preliminary component build-up drag method in the MATLAB framework for preliminary performance estimation and sizing, and through a more accurate FlightStream CFD simulation for verification. Furthermore, the drag polar for this year's aircraft will be computed twice: once for the clean aircraft in $M1$ and $M2$, and once for the aircraft towing the sensor in $M3$ to include the sensor parasite drag.

Basically, the MATLAB framework outputs the parasite drag on the individual components of the aircraft, and the overall aircraft parasite drag is their sum. The induced drag is then computed as a function of the aircraft C_L , hence the aircraft's velocity in different modes of the competition. A more detailed discussion of the drag calculation is demonstrated in the following subsections.

Towed-Sensor Drag

Calculating the parasite drag on the sensor was done using approximating the sensor body to that of a rocket and using the approach of calculating the parasite drag on the rocket body, used in [2], for calculating the parasite drag on the sensor with the stabilizing fins.

$$Cd_f = C_{fc} \times \left[\frac{\left(1 + \frac{1}{2fb}\right) \times S_{wet,body} + \left(1 + \frac{2t}{c}\right) \times S_{wet,fins}}{A_{BT}} \right] \quad (4.9)$$

This technique was utilized in the conceptual design phase to favor one stabilizing surface over the other based on the overall drag coefficient. Thus, for a preliminary sensor length of 27.56 in at a cruising speed of about 82.02 ft/s, the parasite drag coefficient for the sensor can be given by (4.10)

$$C_{D_0(\text{sensor})} = 0.0257 \quad (4.10)$$

Parasite Drag Estimation

Parasite drag for the aircraft individual components was computed using the MATLAB framework, which utilized *the Raymer's book (Aircraft Design) [3]* formula (4.11) for the build-up drag method. In this approach the parasite drag is based on the estimation of flat plate skin friction coefficient over the surfaces exposed to the airflow and is then corrected using the form factor to compensate for pressure drag due to airflow separation and the interference factor to compensate for components' interference effect.

$$C_{D_0} = \frac{C_f \times FF \times Q \times S}{S_{ref}} \quad (4.11)$$

Table 4.3 below demonstrates the code output for the preliminary parasite drag estimation for each component.

Table 4.3: Preliminary Parasite Drag

Components	C_{D_0c}	
	Mission 2	Mission 3
Fuselage	0.0084	0.0087
Vertical tail	0.0014	0.0015
Horizontal tail	0.0028	0.0029
Wing	0.0121	0.0125
Landing gear	0.0105	0.0105
Sensor	–	0.0257
Total	0.0352	0.0618

The pie charts in figure 4.7 illustrate the contribution of each component in the overall parasite drag.

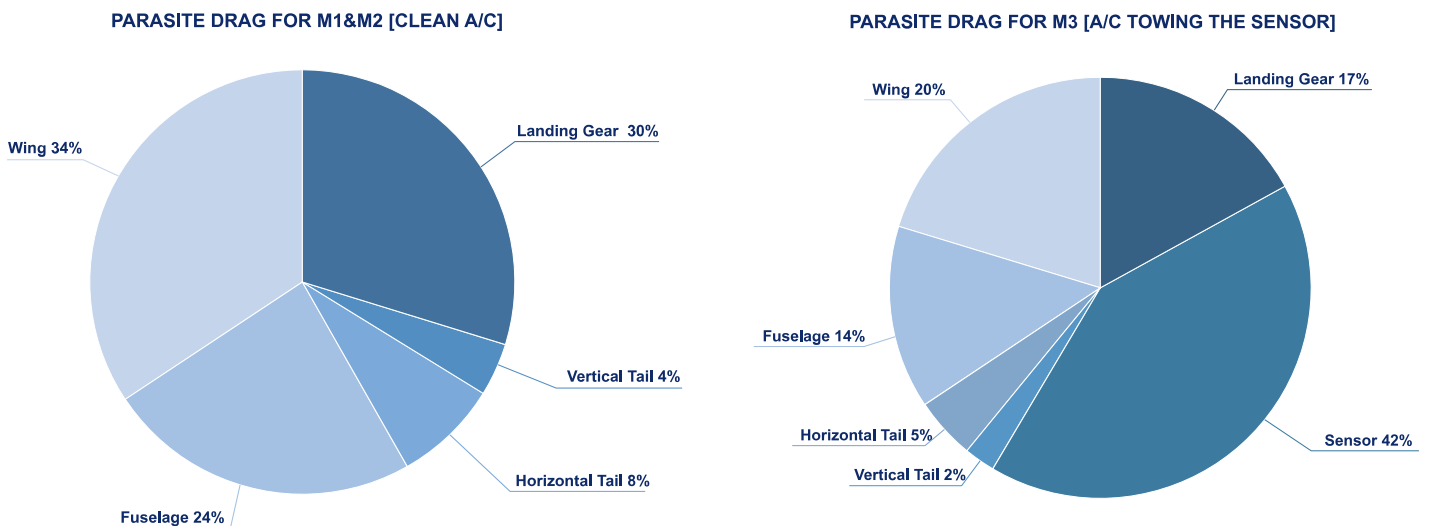


Figure 4.7: Parasite Drag Pie-chart

Drag Polar

The overall drag on the aircraft is the summation of the induced drag and the parasite drag on the aircraft in different mission modes. Hence, the calculated parasite drag coefficient computed in the previous subsection in addition to induced drag formula, which is a function of the C_L , are used to compute the drag polar for each mission in the competition. *Equation (4.12)* represents the drag polar for the aircraft in $M1$ and $M2$, while *equation (4.13)* represents the drag polar for the aircraft during $M3$ with the towed sensor. *Figure 4.8* demonstrates the drag polar of the aircraft in different missions.

$$C_D|_{M1\&M2} = 0.0531 - 0.0426C_L + 0.036C_L^2 \quad (4.12)$$

$$C_D|_{M3} = 0.0797 - 0.0426C_L + 0.036C_L^2 \quad (4.13)$$

CFD Analysis

For a more reliable drag calculation, FlightStream CFD simulation software was later used to calculate the parasite drag coefficient for each individual component as a mean of verification of the results obtained by the MATLAB framework. The obtained data from both the CFD analysis and the designed framework for the parasite drag coefficients for $M2$ are shown in *table 4.4* and for the towed sensor in *table 4.5*; the CFD results are obtained at a zero AoA, with a cruising speed of about 98.4 ft/s for the whole aircraft in $M2$ and 82.02 ft/s for the sensor in $M3$. It is worth noting the results obtained using the CFD simulation and the component build-up drag method were very close as shown below. *Figure 4.9* and *Figure 4.10* illustrates the pressure contour for the aircraft and the sensor, respectively.

Table 4.4: Parasite Drag Coefficient for M2

	C_{D_0} (MATLAB)	C_{D_0} (CFD)
Fuselage	0.0084	0.0097
Vertical tail	0.0014	0.001
Horizontal tail	0.0028	0.0013
Wing	0.0121	0.0093
Landing gear	0.0105	0.0105
Total	0.0352	0.0318

Table 4.5: Parasite Drag Coefficient for M3

C_{D_0} (\approx rocket body)	C_{D_0} (CFD)
0.0257	0.0252

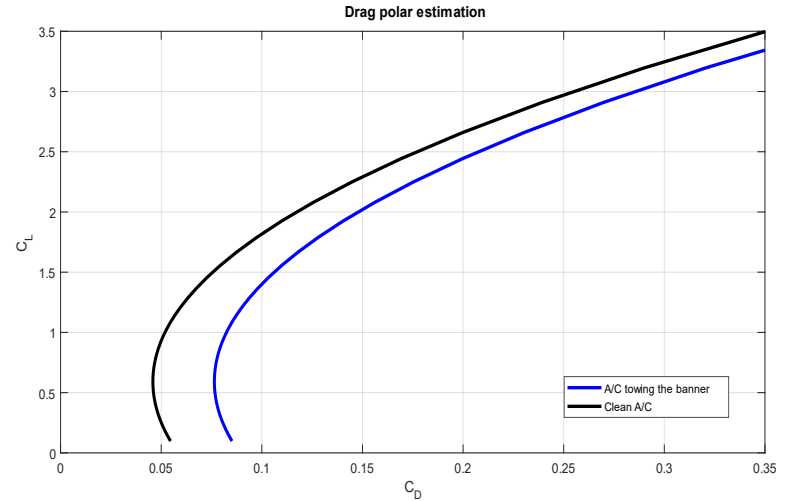


Figure 4.8: Drag Polar Estimation

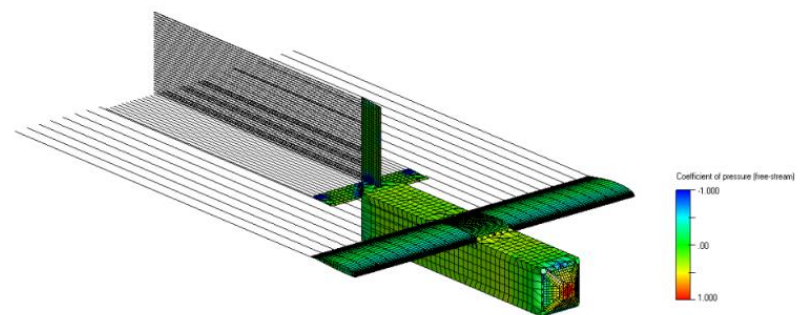


Figure 4.9: Pressure Contour of the Aircraft

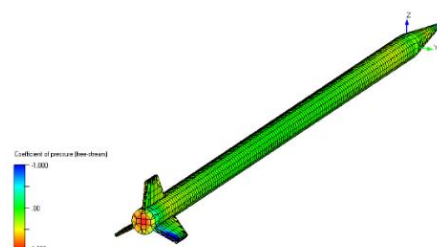


Figure 4.10: Pressure Contour of the Sensor

4.5 Stability and Control

The designed aircraft must meet the stability and controllability requirements for successful mission completion. Hence, after sizing the whole aircraft using the MATLAB framework, iterations using the AVL software are utilized to verify the stability characteristics of the aircraft as a whole in different modes. Moreover, the sizing of the empennage assembly itself is crucial for the static stability of the aircraft; hence, before the AVL stability analysis step, the code iterations are based on finding the dimensions that best achieves properly sized horizontal and vertical tails that meets the desired stability criteria. The stability and control achievement and verification are thoroughly discussed in the upcoming subsections.

4.5.1 Longitudinal Static Stability

Tail Sizing

For achieving the desired longitudinal stability, the MATLAB framework iterates to output the vertical and horizontal tail dimensions and the tail arm that ensures a positive C_{m_0} and a negative C_{m_α} (slope). This is computed using the desired V_h and V_v , AR , S , and $\frac{S_h}{S}$ as inputs. Moreover, the chosen airfoil chosen for both the vertical and horizontal tail is the NACA 0009 for its simple geometry with suitable aerodynamic characteristics for the tail.

Hence, for a horizontal tail volume coefficient of 0.5, a vertical tail volume coefficient of 0.05, $\frac{S_h}{S}$ of 0.20, and an aspect ratio of three for both the vertical and the horizontal tail, the framework yields the dimensions shown in *figure 4.11* for the vertical and horizontal tail with a -3.1221° horizontal tail incidence angle. It is worth noting that the inputs to the code were obtained from collected UAVs database and previous experience in the field and were chosen to serve a specific purpose determined by the team.

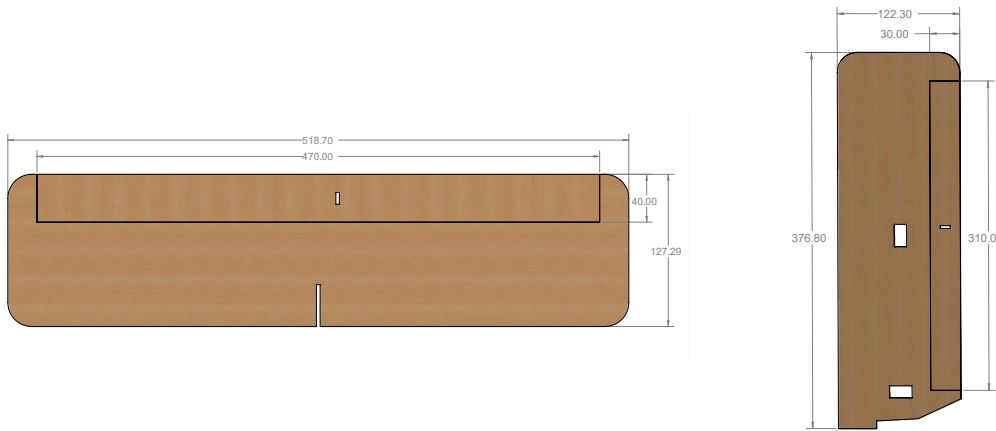


Figure 4.11: Horizontal and Vertical Tail Dimensions

Control Surfaces Sizing

Researching and collecting data for similar UAVs of the same scale yielded a range for the basic design parameters' value for the aileron, elevator, and rudder. Ratios that relate the main control surfaces' parameters and the wing and tail dimensions, which achieve the desired controllability, were taken from [4], and are tabulated in *table 4.6* below. Unlike the whole aircraft sizing and stability analysis, the control surfaces were sized separately using the ratios, and are not included in the MATLAB framework.

Table 4.6: Aileron, Elevator and Rudder Sizing Parameters

Aileron	Elevator	Rudder
$S_a/S = 0.11$	$S_E/S_h = 0.25$	$S_R/S_v = 0.25$
$b_a/b = 0.3$	$b_E/b_h = 0.9$	$b_R/b_V = 0.85$
$\delta_{A_{max,up}} = 25$	$\delta_{E_{max,up}} = 25$	$\delta_{R_{max,right}} = 30$
$\delta_{A_{max,down}} = +20$	$\delta_{E_{max,down}} = 20$	$\delta_{R_{max,left}} = 30$
$b_{ai}/b = 0.7$		

Those ratios were utilized to obtain the preliminary sizing for the aileron, elevator, and rudder in this year's aircraft. The sizing parameters for each of the control surfaces are shown in *table 4.7* below.

Table 4.7: Aileron, Elevator, and Rudder Dimensions

Aileron	Elevator	Rudder
$S_a = 0.05$	$S_E = 0.02$	$S_R = 0.01$
$b_a = 0.45$	$b_E = 0.47$	$b_R = 0.31$
$C_a = 0.11$	$C_E = 0.04$	$C_R = 0.03$
$\delta_{A_{max,up}} = 25$	$\delta_{E_{max,up}} = 25$	$\delta_{R_{max,right}} = 30$
$\delta_{A_{max,down}} = +20$	$\delta_{E_{max,down}} = 20$	$\delta_{R_{max,left}} = 30$
$b_{ai} = 1.05$		

Static Margin and CG Location

The stability analysis in the MATLAB framework for the aircraft in each flight mission utilized AVL software. The static margin, however, was needed as an input to start the iterations. After researching, it was found that a well-behaved aircraft typically has a static margin in the range of 5% to 25%, as this is suggested to provide good stability characteristics. And hence, a static margin of 20% was chosen. The static margin, by definition, is given by *equation (4.14)*

$$SM = \frac{X_{NP} - X_{CG}}{MAC} \quad (4.14)$$

Hence, keeping the center of gravity constant in all flight missions with the constant predetermined static margin deemed the necessity of a constant neutral point in all the missions. AVL, in turn, provides the required elevator deflection in each flight mission that achieves the desired constant neutral point. *Table 4.8* shows the required elevator deflection for each flight mission for a static margin of 20% and X_{CG} of 0.0689 measured from the leading edge of the aircraft.

Table 4.8: The Required Elevator Deflection

Mission	Elevator deflection
M2	0°
M3	-0.32634°

In conclusion, the aircraft sizing and evaluation demonstrates acceptable static stability in all flight missions, as shown in *figure 4.12* below, a suitable trimming angle is achieved with a negative $C_{m\alpha}$ (slope) in each of the missions.

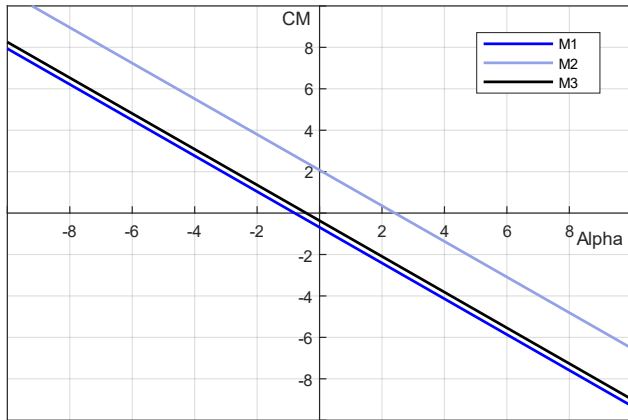


Figure 4.12: C_m Versus α Curve

Table 4.9: Trim AoA for each Mission

	M2	M3
α_0	2.4119°	0.4260°
$c_{m-\alpha}$	-0.8604	-0.8623
c_{m_0}	2.0751	-0.3673

4.5.2 Dynamic Stability

To ensure that the aircraft's behavior is thoroughly studied, the dynamic stability of the aircraft in the three flight missions was also analyzed using XFLR5. As shown in *figure 4.13* below, the dynamic stability of the aircraft can be visualized on the complex plane by plotting the roots of characteristic equations representing the different modes of the aircraft: Phugoid and Short Period (longitudinal modes), as well as Spiral, Roll and Dutch Roll (lateral modes). For a mode to be stable, its real eigen vector real part should be negative, and as shown in the pole zero diagram below all the longitudinal modes for the aircraft in all missions are stable as well as the lateral modes except for the spiral mode as it has a positive pole.

Adding dihedral to the wing has been considered by the aerodynamics sub-team as a mean of increasing stability in the spiral mode because it would increase the spiral mode's time constant. As a result, this would increase the probability that the pilot input will be able to intervene before the aircraft divergence. Nonetheless, the pilot deemed the modification unnecessary, and the spiral mode in *M3* has 8.228 sec. before doubling the amplitude, which is the minimum in all missions, and as stated by the pilot would be enough for his intervention. Moreover, the manufacturing sub-team explained that this modification would only add more complexity to the manufacturing process and is unnecessary. Consequently, the dihedral was not added.

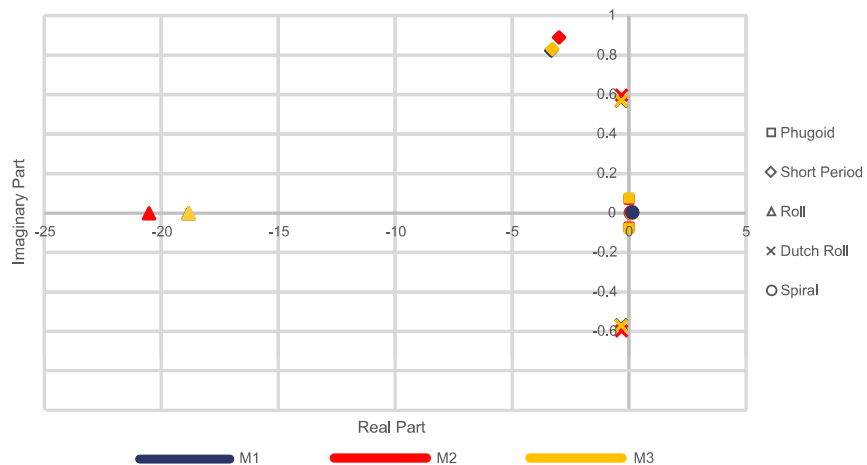


Figure 4.13: Pole-Zero Diagram

In addition, *figure 4.14* below demonstrates the time response of all the modes in all missions.

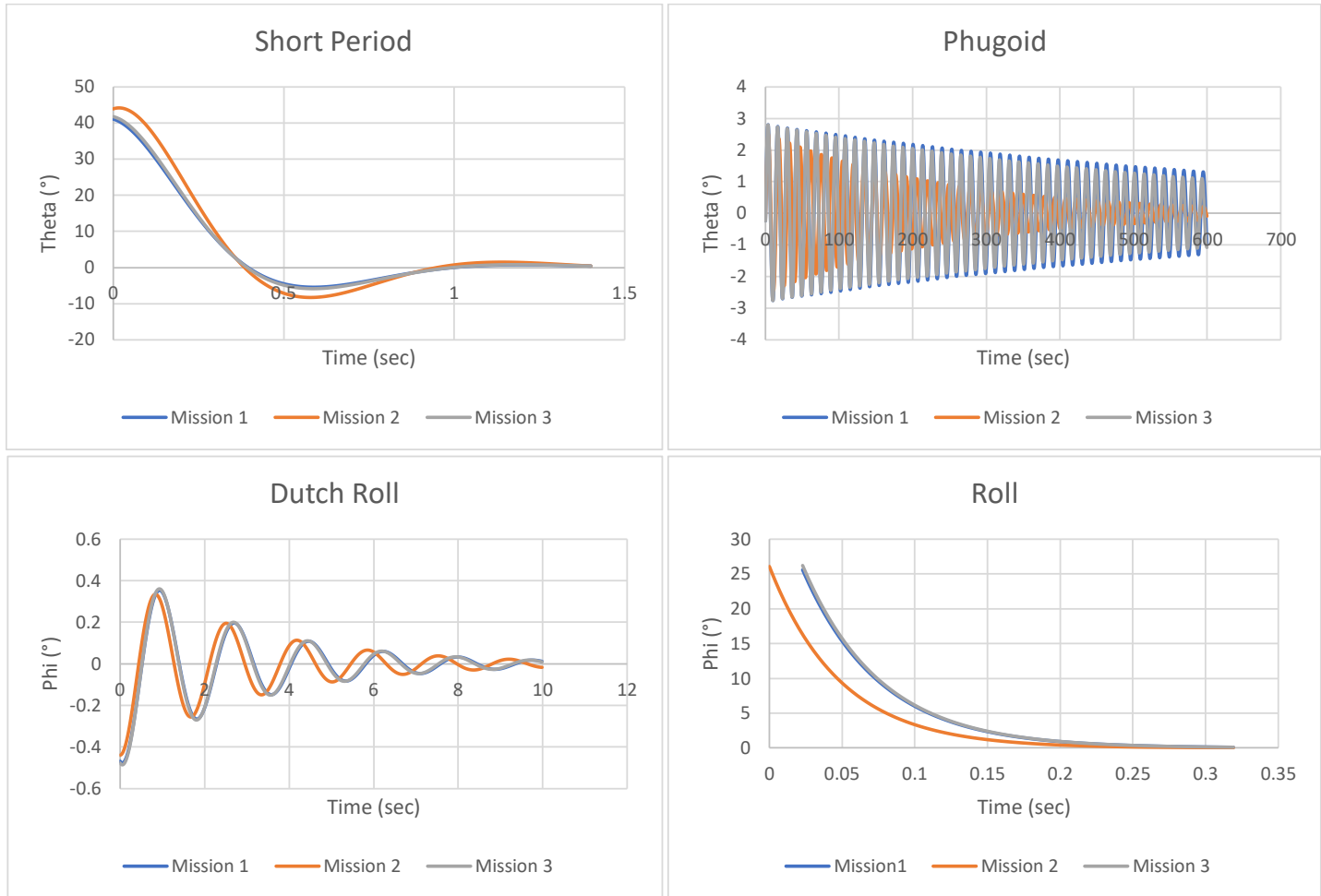


Figure 4.14: Time Response Plots

The dynamic stability modes damping ratio, undamped natural frequency, damped frequency, time constant, and time to double amplitude for unstable poles or time for half amplitude for stable poles were obtained and compared to the acceptable ranges.

Table 4.10 demonstrates the acceptable range for the different modes as specified in [5], and as can be shown in *table 4.11* all the modes for this year's aircrafts lies within the acceptable range of class I level 1, except for the phugoid and spiral modes; they were, however, within the acceptable ranges for class I level 2. Hence, there will be enough time for the pilot to recover the aircraft.

Table 4.10: Acceptable Ranges for Each Mode

Mode	ζ	ω_d (Hz)	τ_R	t_2 or $t_{1/2}$ (sec.)
Short period	0.35 – 1.3	–	–	–
Phugoid	>0.04	–	–	–
	0 (lvl 2)			
Spiral	–	–	–	>12
	–	–	–	>8 (lvl 2)
Roll	–	–	<1.4	–
Dutch Roll	>0.08	>0.159	–	–

Table 4.11: Dynamic Stability Characteristics for Each Missions

Mode	Mission 1 (Empty Weight)					Mission 2 (Full Payload Installed)					Mission 3 (Sensor towed)				
	ζ	ω_n (Hz)	ω_d (Hz)	$t_{1/2}$ or t (sec.)	TR	ζ	ω_n (Hz)	ω_d (Hz)	$t_{1/2}$ or t (sec.)	TR	ζ	ω_n (Hz)	ω_d (Hz)	$t_{1/2}$ or t (sec.)	TR
Short period	0.541	0.980	0.824	—	—	0.472	1.010	0.891	—	—	0.531	0.982	0.832	—	—
Phugoid	0.003	0.076	0.076	—	—	0.009	0.069	0.069	—	—	0.003	0.076	0.076	—	—
Spiral	—	—	—	8.395	—	—	—	—	9.189	—	—	—	—	8.228	—
Roll	—	—	—	0.037	0.053	—	—	—	0.034	0.049	—	—	—	0.037	0.053
Dutch Roll	0.093	0.569	0.567	—	—	0.086	0.6	0.597	—	—	0.093	0.573	0.57	—	—

4.6 Mission Performance Estimations

The performance of the chosen design was predicted in each mission through the mission model discussed earlier in section 4.2. In addition, the score of each mission was calculated. The results of the calculated parameters which represent the aircraft performance in each mission are shown in table 4.12.

Table 4.12: Calculated Performance of Each Mission

Parameter	Mission 1	Mission 2	Mission 3
$C_{L_{Max}}$	1.6	1.8	1.6
$C_{L_{Cruise}}$	0.179	0.392	0.197
C_{D_0}	0.0423	0.0423	0.0441
$(L/D)_{Max}$	18.628	18.028	18.628
$(L/D)_{Cruise}$	3.425	7.884	3.8
Take-off Distance (ft)	8.14	45.45	8.14
Rate of Climb (ft/s)	28.6	22.9	28.55
V_{Stall} (ft/s)	27.89	45.93	28.8
V_{Cruise} (ft/s)	82.02	98.43	82.02
V_{Turn} (ft/s)	88.18	66.48	88.18
Turning Radius (ft)	76.82	28.03	72.03
Wing Loading [W/S] (psf)	1.5	4.5	1.6
Gross Weight (lbs)	6.93	21.78	7.61
Lap Time (s)	29	29	30

5.0 Detailed Design

5.1 Dimensional Parameters

Table 5.1 illustrates the main dimensions and the characteristic parameters of the final aircraft and the propulsion system.

Table 5.1: Characteristic Parameters of the Final Aircraft

Wing		Horizontal Tail		Motor	
Airfoil	S3002	Airfoil	NACA 0009	Model	Scorpion SII-4035-380
MAC	11.79 in.	MAC	5.01 in.	Kv	380
Span	4.91 ft	Area	0.97 ft ²	I_0	1.52 A
Aspect Ratio	5	Span	1.70 ft	Power	2600 Watts
Area	4.83 ft ²	Incidence Angle	-3.12°	Total Weight	1 lbs

Flaps (Plain)		Elevator		Batteries	
Span	1.08 ft	Span	1.54 ft	Type	LiPo
Chord	3.54 in.	Chord	1.57 in.	Capacity	3000 mAh
Max. Deflection	25°	Vertical Tail		No. of Cells	9
Ailerons		Vertical Tail		I_{Max}	
Span	1.48 ft	Airfoil	NACA 0009	Total Weight	85 A
Chord	4.33 in.	MAC	4.80 in.	Main Landing Gear	
Fuselage		Area	0.48 ft ²	Width	17.812 in.
Length	52.009 in.	Span	1.20 ft	Height	11.089 in.
Max. Width	7.784 in.	Rudder		Ground AoA	
Max. Height	7.784 in.	Span		13°	
Rudder		Chord			

5.2 Structural Characteristics and Capabilities

5.2.1 Layout and Design

For this year's aircraft to meet all the mission requirements, it was essential to take into consideration the necessity of designing a structure that withstands all the predicted loads in the different phases of the competition, while maintaining lightweight, high payload interior capacity and accessibility. To facilitate the designing and testing process, the predicted loads were put into two main categories:

Static Loads:

- Aircraft weight: these include the forces acting on the aircraft structure due to its own empty weight and the weight of the payload installed.
- Aerodynamic loads while cruising: these include the bending and twisting moment generated by the wing and the control surfaces' lift generation in addition to the shear force due to the drag on the aircraft while cruising.

Dynamic Loads:

- Aerodynamic loads while accelerating: these include the forces and moments acting on the aircraft structure in flight i.e. loads imposed on the aircraft structure due to maneuvering in air or landing.
- Propulsive loads: these include the thrust force and the torque on the fuselage generated by the motor in addition to the inevitable generated vibrations during the motor operation.
- Towed-sensor loads: these include the drag and moment generated by the sensor on the aircraft in the different phases of *M3* profile.

As shown in *figure 5.1* below, the structure is designed to transfer all the loads into the major load-bearing component, which is the wing spar frame structure; the propulsive loads and the towed-sensor loads are transferred from the fuselage to the wing spar, while the landing impact is transferred from the landing gears to the fuselage, which in turn transfers them into the wing spars. Hence, the fixation of the wing spar with the fuselage was thoroughly studied to ensure it withstands this load transfer, and the landing gears fixation was also reinforced to damp the landing impact. Details on the aircraft structure are presented in *section 5.3*.

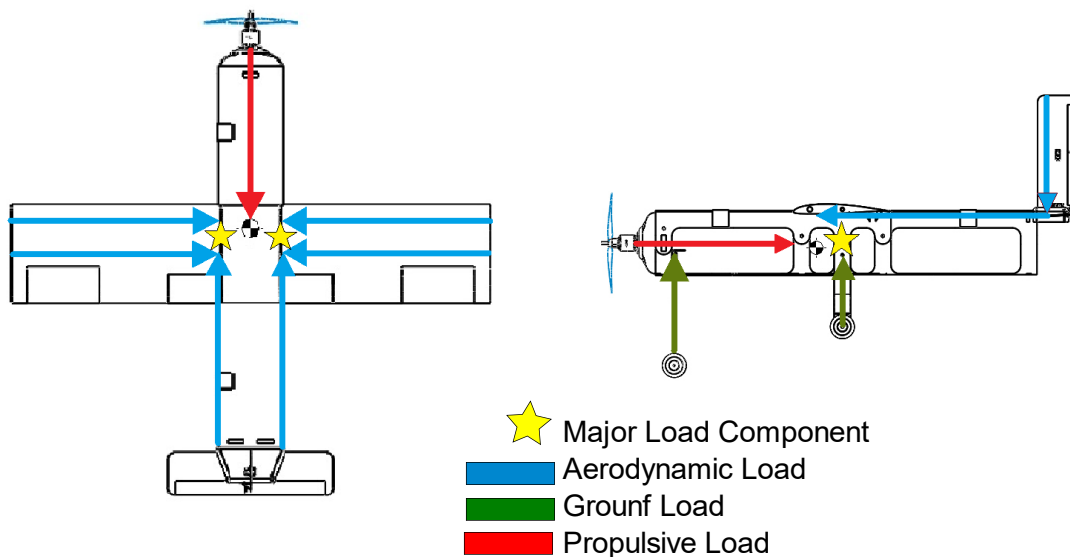


Figure 5.1: Load Paths of Major Forces

5.2.2 Flight Envelope

The aircraft is designed to withstand, theoretically, up to $9g$ loading factor to meet the maximum expected loading among all missions. In addition, the V-n diagram in *figure 5.2* below demonstrates the operational flight envelope for the aircraft after analyzing the different flight mission stages. Hence, this year's aircraft with 9.73 lb empty weight safely accommodates 5.25 lb payload while sustaining $5g$ turns with a banking angle of 78.46° .

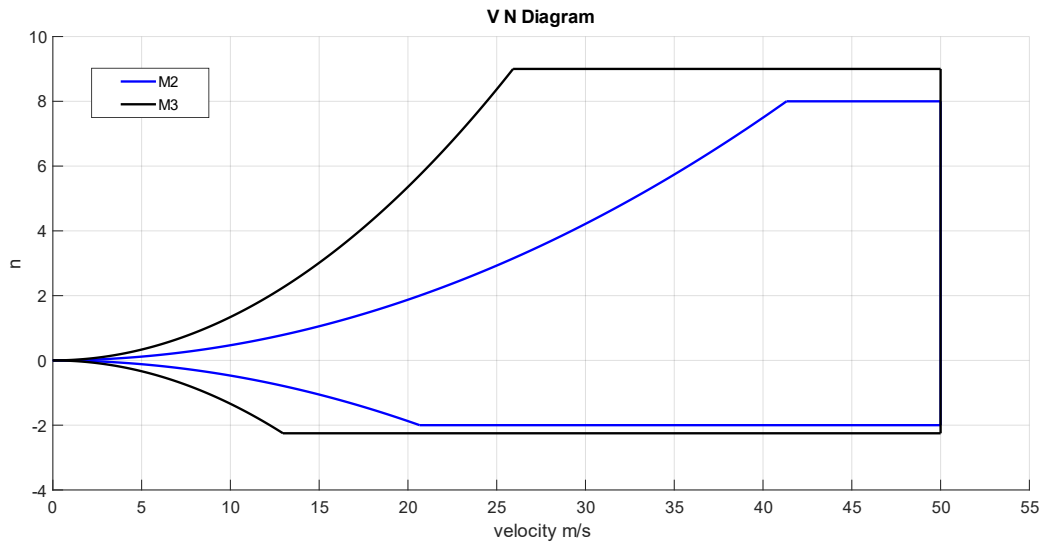


Figure 5.2: Flight Envelope Diagram

5.3 Subsystems Design

Delivering the desired performance and meeting the required structural strength while utilizing the most efficient and accessible techniques was the pre-eminent purpose in the aircraft sub-systems design. Multiple design iterations were implemented for each sub-system until the final material and structural design were converged. The following sections document the detailed description of the major aircraft sub-systems.

5.3.1 Wing Structure

The wing was designed to carry flight loads while minimizing the weight. A blue foam core wing supported by two metallic spars was chosen. Considering that most of the load is concentrated at quarter the chord: $0.63\text{-inch-diameter}$ stainless steel spar was chosen due to its high bending strength. Besides, due to its lightweight, a $0.47\text{-inch-diameter}$ aluminum spar was mounted 3.94 in. away from quarter the chord, the selection was based on previous data from the past years. The wing is connected to the fuselage utilizing a plywood connector, which is then fixed to the fuselage by screws. The wing structure is illustrated in *figure 5.3* below.

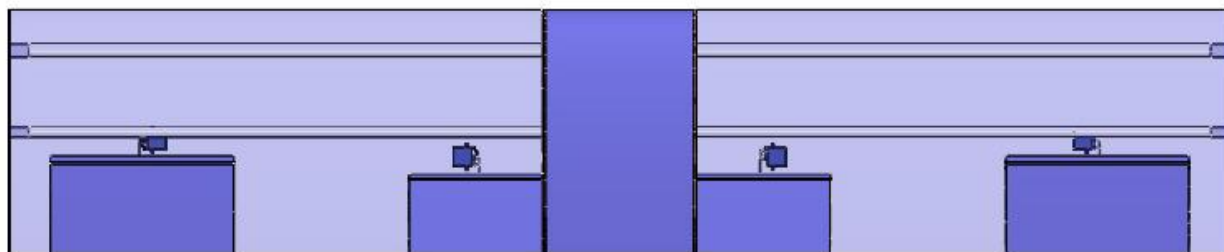


Figure 5.3: Wing Structure

5.3.2 Fuselage Design

The fuselage was designed to be lightweight, implement ample space for the payload, and endure severe flight loads. In order to withstand the impact load from the landing gear as well as the torque from the motor, the main structure of the fuselage was made of hollow plywood—to decrease weight, as shown in *figure 5.4*. Additional strengthening components are situated in the areas that are loaded the most that needed to be completely fixed; thus, structural rigidity is guaranteed. These components are listed below:

- 0.12-inch-thickness plywood ribs at the two sides of the fuselage connecting the motor mount to the wing.
- 0.12-inch-thickness plywood cell at the fuselage bottom connecting the motor mount to the landing gear.

Pieces of blue foam are placed on the interior sides of the fuselage to keep the containers stable and immovable. The skin of the fuselage is made of white foam, due to its lightweight and ease of manufacturing.

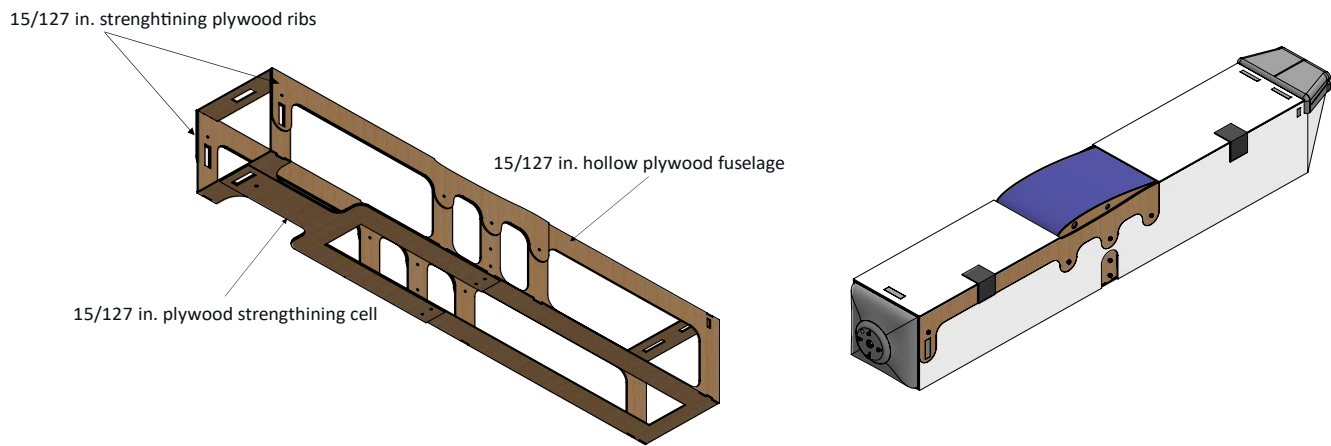


Figure 5.4: Fuselage Interior Structure

5.3.3 Landing Gear Design

The landing gear is in a tricycle configuration, as illustrated in *figure 5.5*. This design prevents the large propeller from hitting the ground; besides, the main landing gear is split into two sections, leaving space for the mechanism door slot. Moreover, this configuration provides the most effective controllability relative to the other configurations. The landing gear leg is made of a thin strip of aluminum due to its high strength to weight ratio, in addition to being easily shaped.

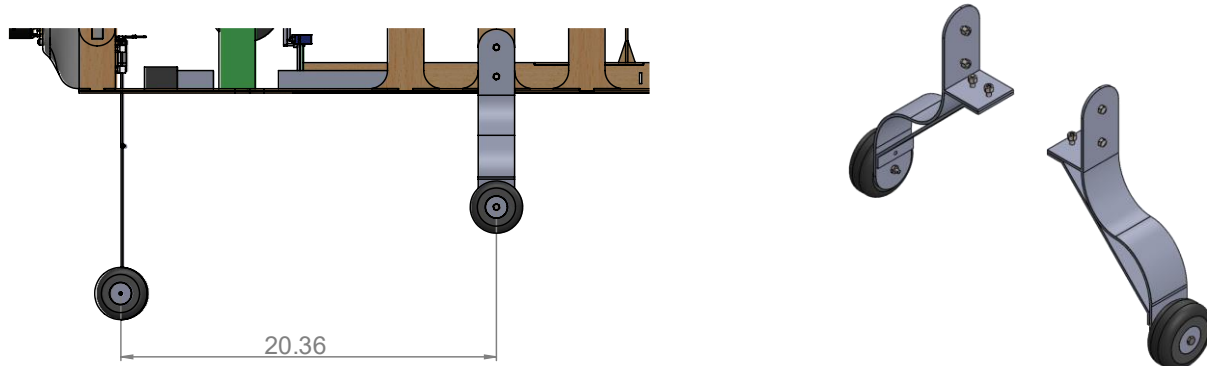


Figure 5.5: Landing Gear Design

5.3.4 Empennage Design

A conventional plywood built-up structure was used for the tail. The conventional configuration gives the most beneficial landing and takeoff capabilities. It consists of two flat plates connected via a 3D-printed-PLA+ tail connector, possessing high rigidity and toughness, that is made to withstand the bending moment arising from the tail. Aluminum hinges will be used as elevator and rudder hinges to guarantee reliable and smooth control. The full empennage assembly is shown in *figure 5.6*.

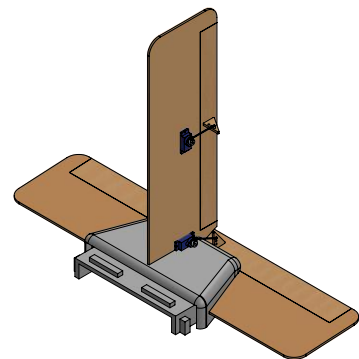


Figure 5.6: Tail Assembly

5.3.5 Servo Selection

Two main types of servos shown in *figure 5.7* are used in controlling the aircraft; they are used according to the loads each must support. First, FS90MG servos are reliable for actuating the control surfaces as well as the deployment and recovery mechanism door. Moreover, the FS5106R servo—specifically for continuous rotation—is used for the deployment mechanism pulley.



Figure 5.7: Selected Servos

5.3.6 Receiver and Transmitter Selection

Spectrum AR9020 was selected to be the main receiver of the aircraft and Spectrum DX9 as its transmitter; both of which would be used to control the main aircraft control surfaces – ailerons, elevator, and rudder – as well as the throttle and the deployment and recovery mechanism. In addition, the second receiver was selected to be AR8000 spectrum—more compact than the AR9020 as it will be attached next to the mechanism's ratchet pulley—and its DX8 spectrum receiver, which will be used to monitor the LED pattern. AR8000 has 8 channels; one will be used to power the receiver, and another one to control the LED signal; therefore, there are 6 redundant channels; however, that is the smallest receiver available in the lab.

5.3.7 Payloads

Sensor

The designed sensor, as shown in *figure 5.8*, is mainly a hollow-metallic cylinder, with three cuts replaced by 3D-printed parts, where these 3D-printed parts are the housing units for the LEDs. The base and the cover are, also, 3D-printed. The base is attached to the metal cylinder using double face tape, and the cover is the housing unit of the batteries.

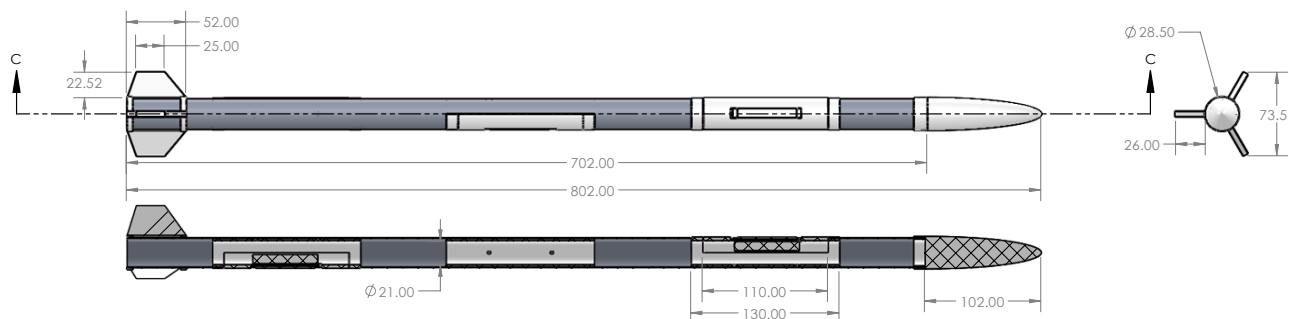


Figure 5.8: Sensor Design

Sensor deployment/recovery mechanism

A reliable mechanism is crucial, in order to have a successful attempt in *M3*. Two different mechanisms were designed and tested throughout the process. The chosen mechanism is a balsa-built structure. As seen in *figure 5.9*, it comprises a ratchet pulley, two servo motors, and a DC motor. Using an electric wire wrapped around the pulley, the mechanism is connected to the sensor inside the shipping container during flight. The electric wire serves as the only physical connection between the aircraft and the sensor. Also, it is used to supply the LEDs with power. Moreover, the pulley will be attached to a separate battery and receiver – apart from the aircraft receiver controlling the servos– on the side face.

In order to open the mechanism's door, a 180-degree servo motor will drive solid plastic arms, each connected to a pin moving through a slot to open the two doors concurrently– to ensure the door's rigidity– causing the sensor to be deployed. The DC motor rotates the pulley for recovery, dragging the sensor back to its original position; afterwards, the door is closed remotely. The mechanism was favored because it was easier to be manufactured and more controllable since the sensor was held from its CG.

Containers

The rectangular-shaped box, shown in *figure 5.10*, was chosen for the container's configuration. It is made of white foam to withstand shocks and protect the sensor efficiently beside being light in weight. Furthermore, five shaped blue-foam supports were attached to the container's walls to center the sensor, prevent its movement, and increase its stability during *M2*. The container is locked using Velcro strips.

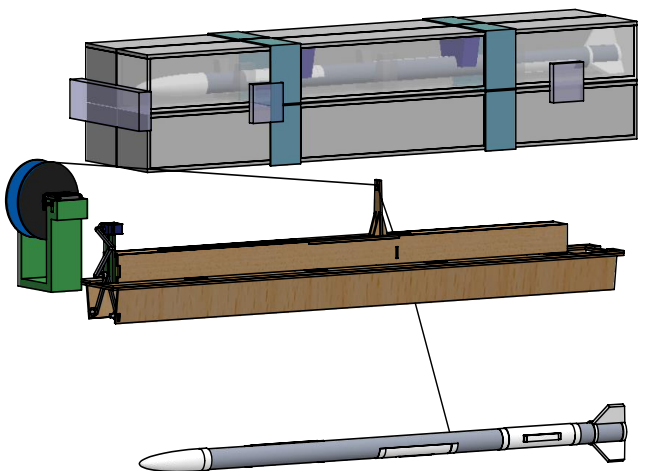


Figure 5.9: Deploying/Recovery Mechanism

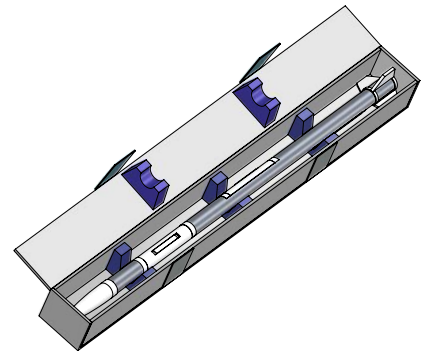


Figure 5.10: Container Design

5.3.8 Propulsion System

The performance of many combinations was estimated using the MATLAB framework, as described in *subsection 4.3.20*. Among the resulting systems, the lightest one was chosen. In addition, A Scorpion Tribunus-12 130A ESC was added to the system to maintain the maximum drawn current during *M2*. In order to prevent the batteries explosion during flight, the propulsion system must include a fuse to open the circuit when the consumed current exceeds the maximum discharge current rating of the batteries. Based on the capacity of the selected batteries and the expected maximum currents, a Blue Midi 0-378-20 fuse was chosen to cut off the current and activate the safety landing mode for currents more than 100 A.

Afterwards, the system was prepared to be tested in wind tunnel to compare the measured performance with the expected one in order to determine any possible improvements. *Figure 5.11* shows the available and required thrust for each mission. The available thrust curves represent the data collected during the test at 100% and 80% throttle settings. However, the thrust required was calculated for a large range of cruising speeds assuming that it equals the drag on the aircraft obtained in *subsection 4.4.3*.

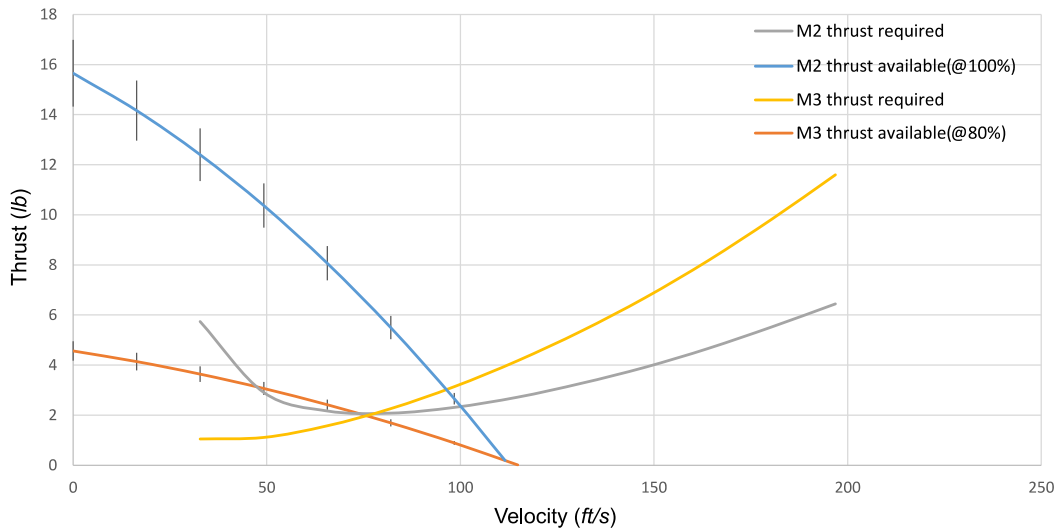


Figure 5.11: Available and Required Thrust for Each Mission

Table 5.2 shows the final propulsion system for each mission. In *M2*, it can provide the required thrust at full throttle setting and the battery will last approximately for 2.3 minutes. While in *M3*, the battery will endure the ten-minute flight window at 80% throttle setting.

Table 5.2: Final Propulsion System for Each Mission

Components	Missions 1&2	Mission 3
Motor	Scorpion SII-4035-380 kv	
Propeller	APC 17x8 E	APC 14x8.5 E
ESC	Scorpion Tribunus 12-130A	
Battery (Series-Connection)	3000mAh LiPo (9 cells)	6000mAh LiPo (6 cells)
Receiver	Spectrum AR9020 (9-Channel)	
Transmitter	Spectrum DX9	
Fuse	Blue Midi 0-378-20	

5.4 Weight and Balance

Specifying the mass and the CG location of each individual component of the aircraft is an essential step in implementing, accurately, the designed aircraft and verifying the predetermined location of its CG during the longitudinal stability study discussed in *subsection 4.5.1*. Moreover, documenting the mass and the CG location of all the components, separately, highlights the impact of each individual component on the whole aircraft CG location in the different flight missions. Hence, SolidWorks software package was utilized to specify the mass and CG location of all the aircraft components included in the final CAD model using the material chosen for each component and its location. Afterwards, the data obtained were tabulated in the weight and balance *table 5.3*.

Table 5.3: Weight and Balance Table

Components	Mass	CG (x – axis)	CG (z – axis)
Units	lb	in	in
Empty Weight			
Fuselage	6.53	0.06	–3.54
Wing	1.03	4.71	–0.15
Motor	0.08	–20.37	–3.82
Propeller	0.01	–22.21	–3.82
H-Tail	0.33	32.27	–0.43
V-Tail	0.23	31.63	6.84
Main Gear	0.86	5.91	–12.13
Nose Gear	0.26	–14.44	–18.15
Total Empty Weight	10.29	0.47	–3.97
Mission 1			
Main Battery	1.92	19.47	–6.56
Receiver Battery	0.01	–12.29	–6.93
Deploy/Recovery Mechanism	1.17	0.28	–5.73
Total Aircraft	13.88	2.69	–4.56
Mission 2			
Main Battery	1.92	–5.44	–7.03
Receiver Battery	0.005	–12.29	–6.93
Sensor	0.53	17.08	–1.97
Sensor Container	0.48	11.83	–1.61
Container Simulators	3.03	14.58	–3.80
Deploy/Recovery Mechanism	1.17	0.28	–5.73
Total Aircraft	17.92	2.72	–4.33
Mission 3			
Main Battery	1.72	16.73	–6.83
Receiver Battery	0.01	–11.89	–6.93
Sensor (inside the aircraft)	0.53	16.65	–6.82
Deploy/Recovery Mechanism	1.17	0.28	–5.73
Total Aircraft (sensor recovered)	14.21	2.67	–4.65

5.5 Flight and Mission Performance

5.5.1 Flight Performance

Table 5.4 shows the flight performance of the final aircraft which is expected using the MATLAB framework.

Table 5.4: Estimated Performance of the Aircraft in Each Mission

Parameter	Mission 1	Mission 2	Mission 3
$C_{L_{Max}}$	1.6	1.8	1.6
$C_{L_{Cruise}}$	0.359	0.3225	0.3684
C_{D_0}	0.0406	0.0406	0.0676
$(L/D)_{Max}$	19.604	14.357	19.604
$(L/D)_{cruise}$	7.3117	4.516	7.864
Take-off Distance (ft)	24.6	45.46	24.9
Rate of Climb (ft/s)	23.62	22.77	23.33
V_{Stall} (ft/s)	38.89	41.65	39.37
V_{Cruise} (ft/s)	82.02	98.43	82.02
V_{Turn} (ft/s)	36.75	67.53	37.09
Turning Radius (ft)	13.32	28.92	12.74
Wing Loading [W/S] (psf)	2.9	3.7	3
Gross Weight (lbs)	13.88	17.92	14.21
Lap Time (s)	29	29	33

5.5.2 Mission Performance

The missions' scores and results are listed in table 5.5. These results were estimated assuming a successful first flight mission with a report score as the past year's score.

Table 5.5: Missions Score Prediction

	M1	M2		M3		GM	
	—	$N_{containers}/T_{M2}$	2.94	$N_{Laps} \times L_{Sensor} \times W_{Sensor}$	2.69	T_{GM}	18
	—	$(N_{containers}/T_{M2})_{Max}$	20	$(N_{Laps} \times L_{Sensor} \times W_{Sensor})_{Max}$	15	$(T_{GM})_{Min}$	9
Mission Score	1	1.15		2.18		0.5	
Total Mission Score		4.83					
Report Score		85					
Total Score		410.55					

5.6 Drawing Package

The following drawing package demonstrates each of the 3-view drawing with each part's dimensions, the structural arrangement drawing, the systems layout drawing, and deployment/recovery mechanism as well as the container simulators compartment (payload accommodation) drawing.

4

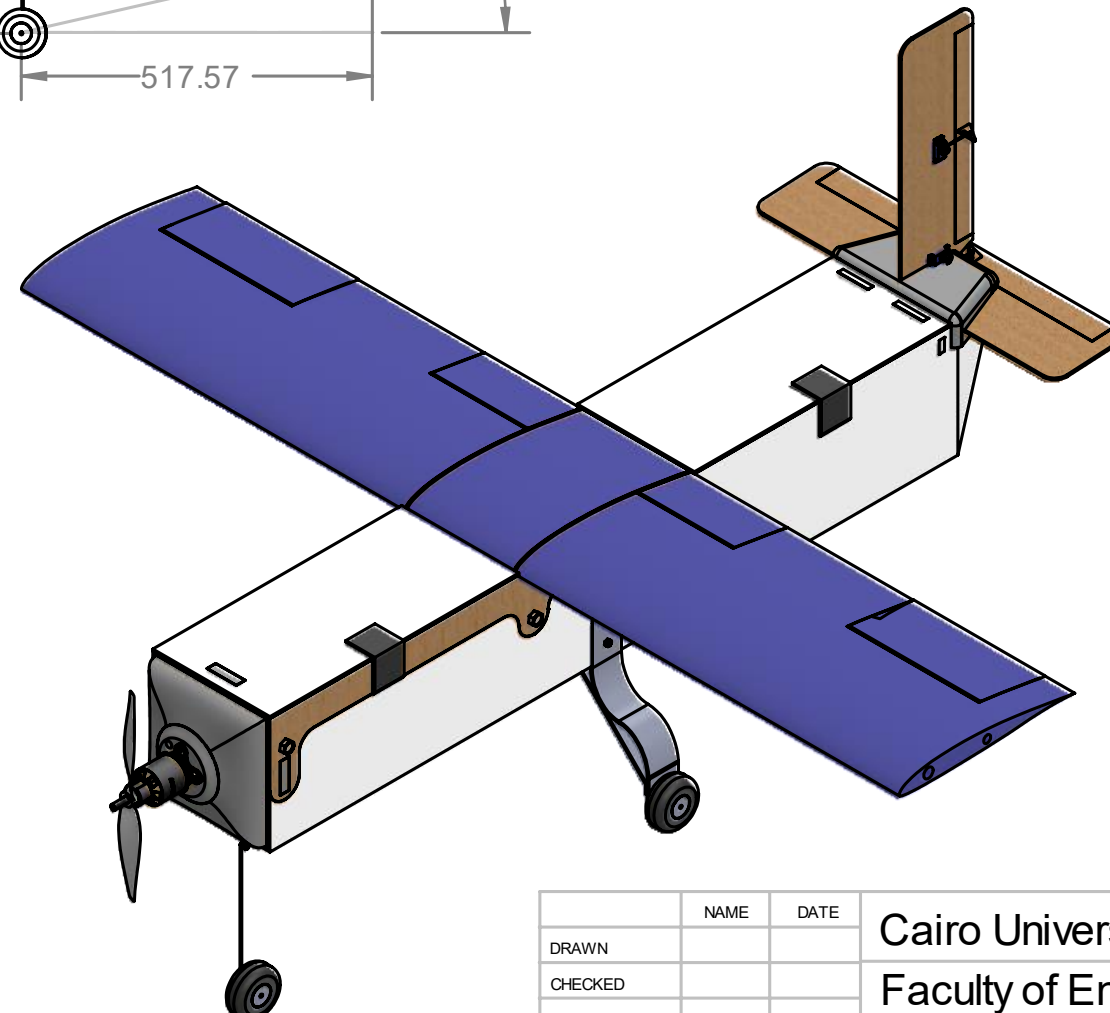
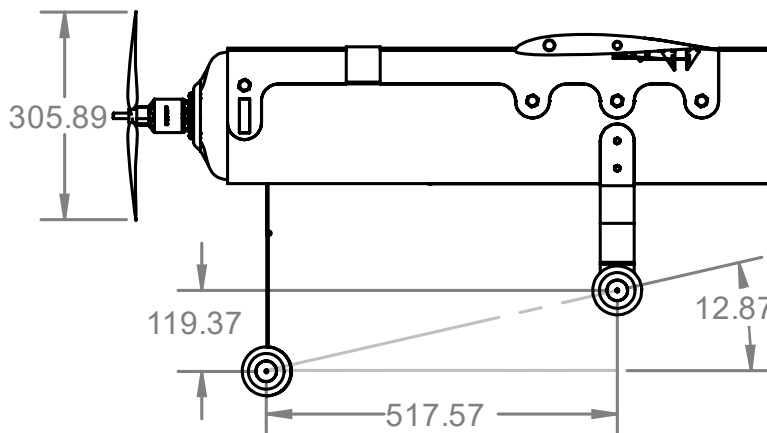
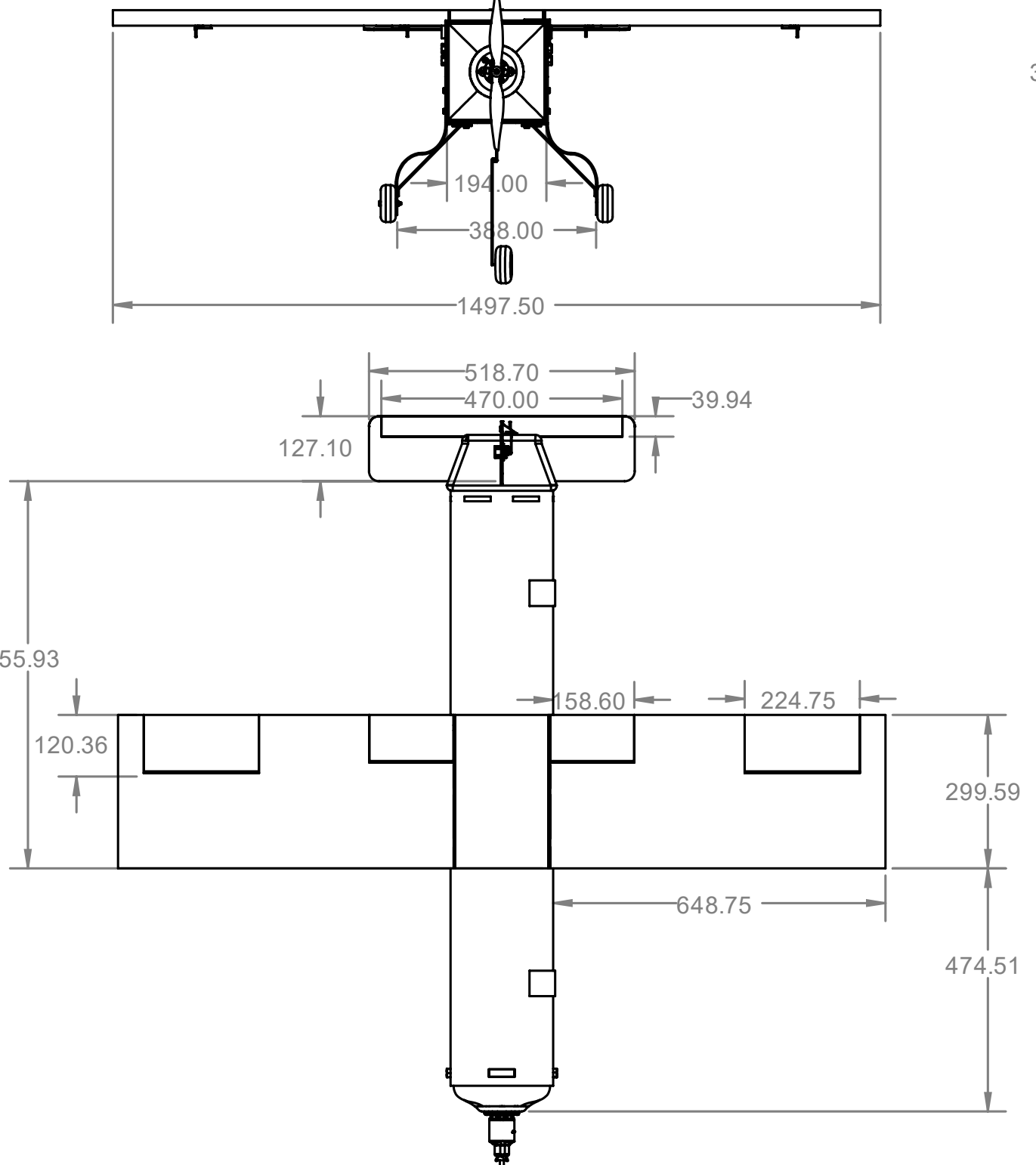
3

2

1

B

B



DRAWN	NAME	DATE
CHECKED		
ENG APPR.		
MFG APPR.		
Q.A.		
Dimensions are in inches		
SIZE	DWG. NO.	REV
B	3-Views	
SCALE: 1:20 WEIGHT: SHEET 1 OF 1		

4

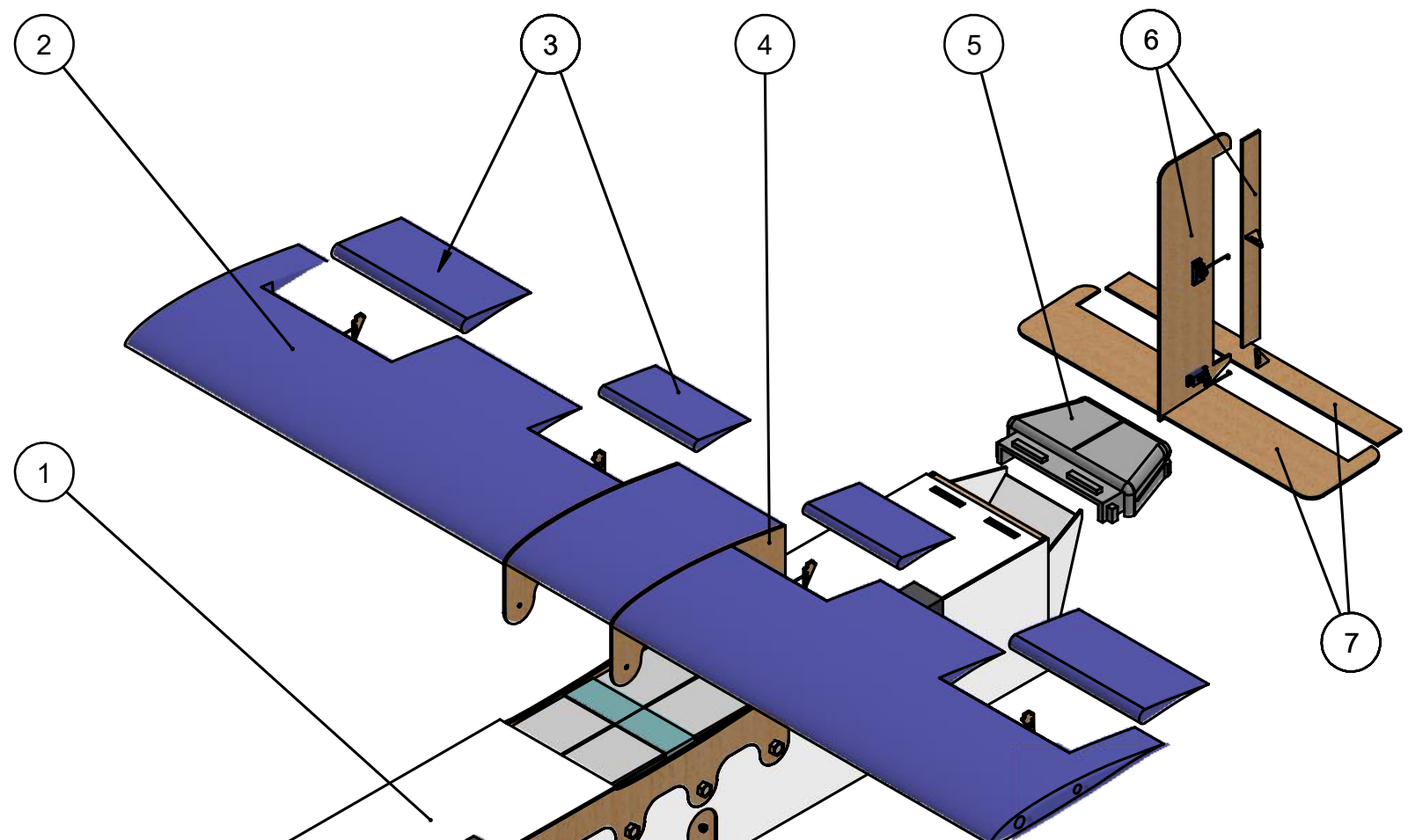
3

2

1

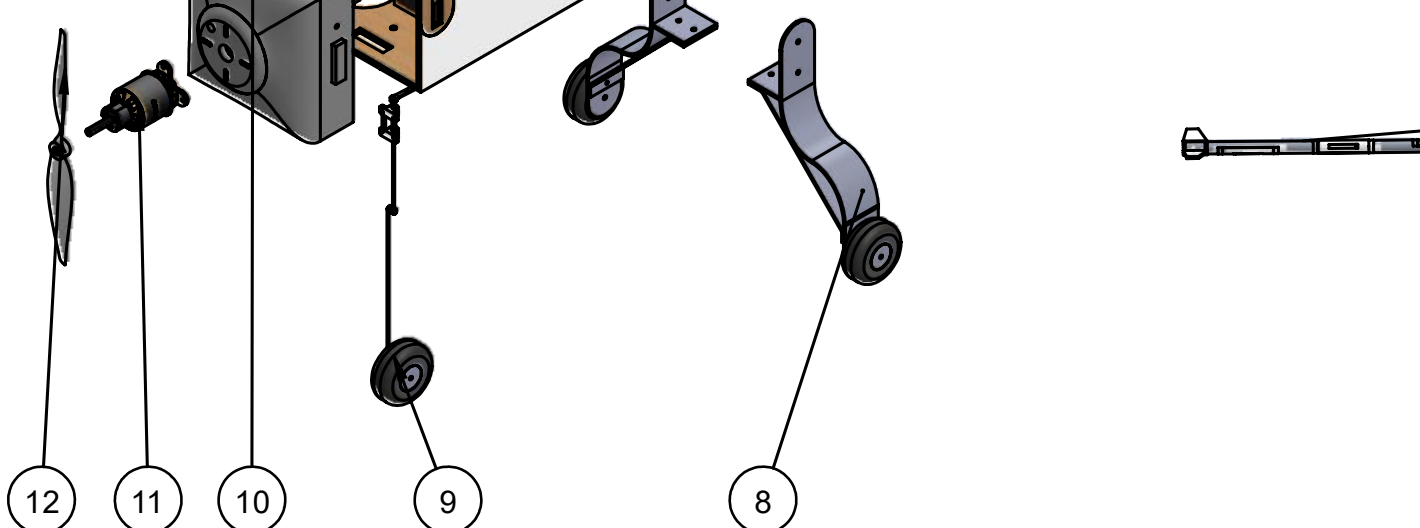
B

B

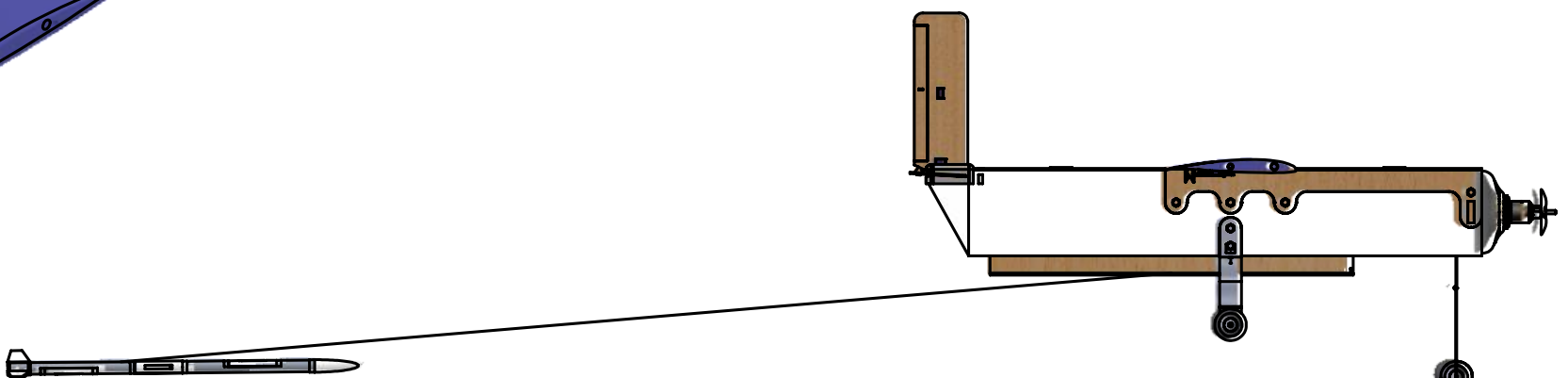


A

A



ITEM NO.	PART NUMBER	DESCRIPTION	QTY.
1	Container	5mm foam	1
2	Wing	Foam, supported with 16mm metal spars	2
3	Ailieron&Flaps	Foam, supported with wooden plates	2
4	Wing connector	Wooden plate	2
5	LEDs	100-Lumens LED lights	1
6	Vertical Stabilizer & Rudder	Wooden plates	1
7	Horizontal Stabilizer & Elevator	Wooden plates	1
8	Main Landing Gear	Aluminum strips, Rubber/Plastic wheel	1
9	Nose Landing gear	Rubber/Plastic wheel	1
10	Motor Mount	3d-printed PLA+	1
11	Motor	Scorpion SII-4035-380Kv	1
39	Propeller	APC 17x8E	1



DRAWN	NAME	DATE
CHECKED		
ENG APPR.		
MFG APPR.		
Q.A.		
Dimensions are in Inches		
SIZE	Exploded	REV
B	view	
SCALE: 1:25 WEIGHT:		SHEET 1 OF 1

4

3

2

1

4

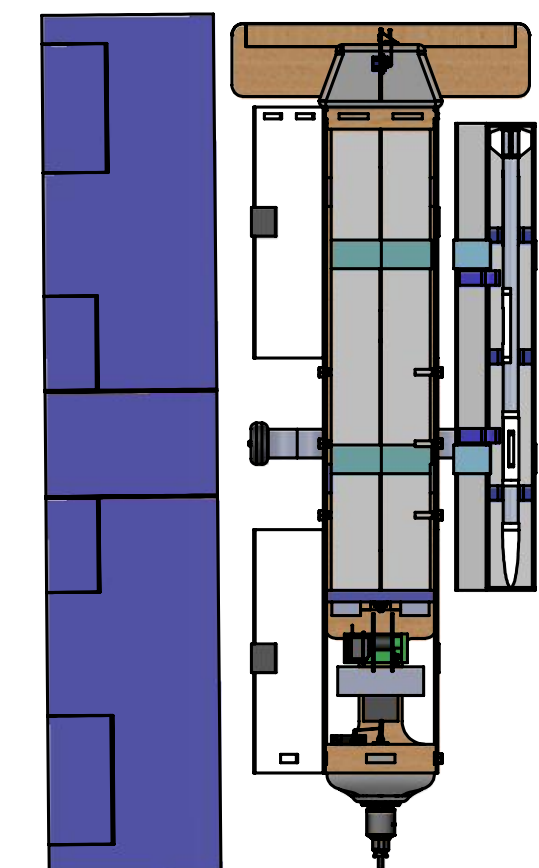
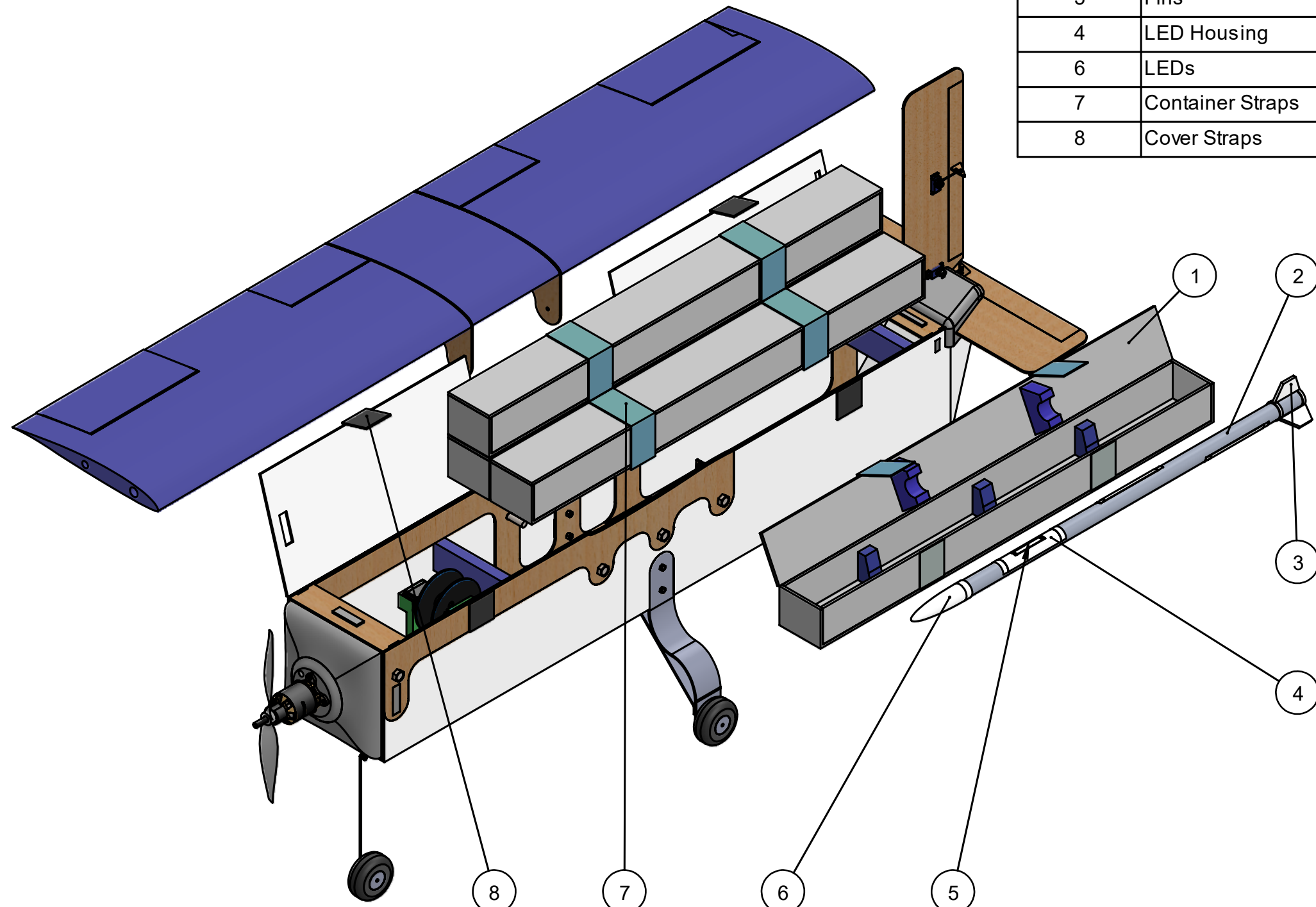
3

2

1

B

B



DATE	Cairo University	
	Faculty of Engineering- Aerospace Department	
UDC Lab		
All Dimensions are in Inches		
SIZE	B Container View	REV
SCALE: 1:20	WEIGHT:	SHEET 1 OF 1

4

3

2

1

4

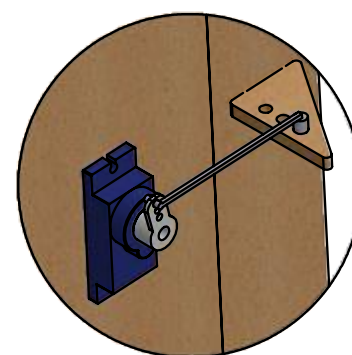
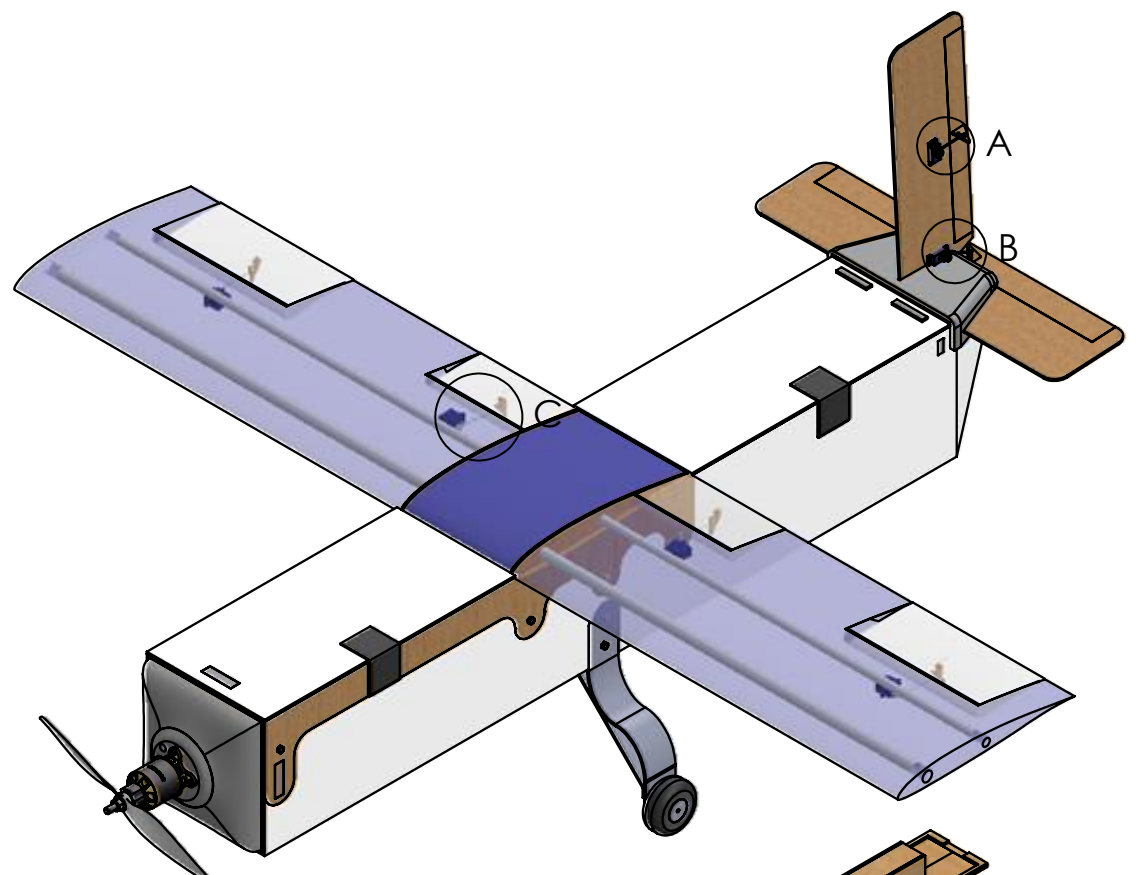
3

2

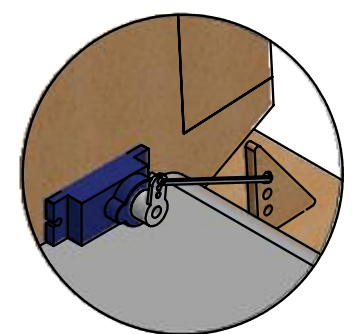
1

B

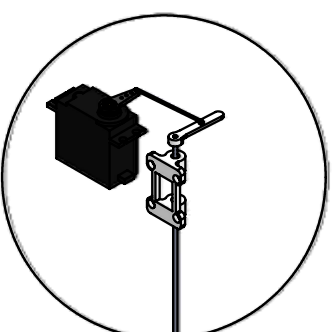
B



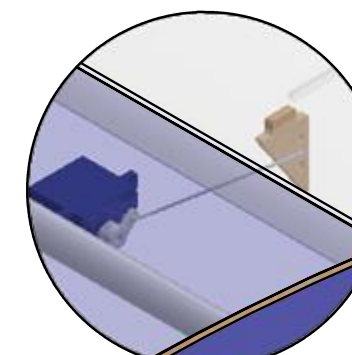
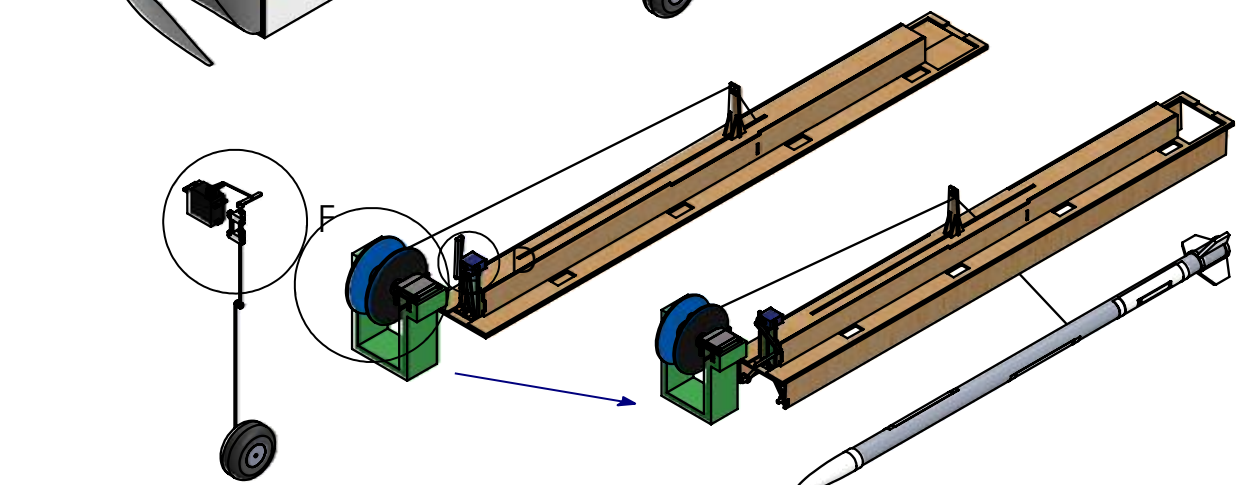
DETAIL A
SCALE 1 : 1.5



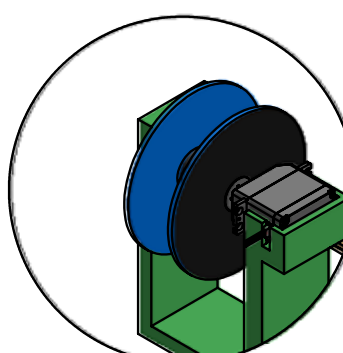
DETAIL B
SCALE 1 : 1.8



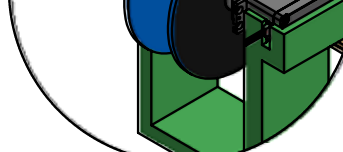
DETAIL F
SCALE 1 : 4



DETAIL C
SCALE 1 : 2.2



DETAIL E
SCALE 1 : 4



DETAIL D
SCALE 1 : 1.6

Item No.	Name	Function
1	Servo motor 1	Controls rudder
2	Servo motor 2	Controls elevator
3	Servo motor 3	controlling ailerons and flaps
4	Servo motor 4	Controlling mechanism doors
5	Servo motor 5	Deploying and recovering sensor
6	Servo motor 6	Controlling nose landing gear

	NAME	DATE	Cairo University	
DRAWN				
CHECKED				
ENG APPR.				
MFG APPR.				
Q.A.				
COMMENTS:				
B SIZE DWG. NO. REV				
payload accommodation				
SCALE: 1:20 WEIGHT:			SHEET 1 OF 1	

4

3

2

1

6.0 Manufacturing Plan

Various manufacturing techniques and materials were explored and compared for manufacturing each component of the aircraft. The criteria of selection included lightweight, low cost, ease of fabrication for rapid prototyping, as well as the team's familiarity and experience with the technique and material of interest. The optimal choice for each individual component was regarded as being the one with the best combination of the aforementioned criteria in accordance with the structural requirements for that specific component. A detailed discussion of the team's manufacturing approach is presented in the following subsections.

6.1 Manufacturing Process Investigated

After researching for the commonly used manufacturing techniques of similar UAVs of the same scale in DBF competitions and other commercial RC planes, the team thoroughly investigated four major techniques: Balsa Build-Up, Plywood, 3D Printing, Foam Core, and composites.

In order to evaluate these four manufacturing techniques, four figures of merit were chosen to represent the key aspects taken into consideration while determining the optimal manufacturing process among them. The weight of each figure of merit reflects its importance and its impact on the overall performance. A score is then given to each technique from one to four and is then multiplied by the weight of the FOM to calculate the total score; a score of 4 means the technique is superior while a score of 1 means the technique is inferior to its counterparts. *Table 6.1* shows the used FOM in evaluation.

- **Lightweight:** since weight directly affects $M2$ and $M3$ score, and higher empty weight translates into higher power consumption and lower payload capacity for the same aircraft size, lower empty weight is pursued, and hence lightweight is given the highest weight: 4.
- **Ease of fabrication:** since this speeds up the manufacturing process and enables rapid prototyping which is needed for multiple testing within the competition's time frame, ease of fabrication was given a weight of 3, as meeting deadlines is a major concern.
- **Previous experience:** since familiarity with the manufacturing technique would add more reliability to the technique and the expected quality out of it, the previous experience was taken into consideration while evaluating the different techniques but was given only a weight of 2, because the team's main aim from participating each year in the competition is to gain new experience and explore newer techniques.
- **Low cost:** since the funding resources are limited, the cost was taken into consideration and was given a weight of 1.

Table 6.1: Manufacturing Process FOM

Figure of Merit	Factor	Balsa Build-Up	Plywood	3D Printing	Foam Core	Composites
Lightweight	4	3	4	1	4	2
Ease of fabrication	3	2	3	3	3	1
Previous experience	2	4	4	3	4	2
Low cost	1	3	4	2	3	1
Total Score		29	37	21	36	16

As shown in *table 6.1* the plywood is the highest-scoring material and was accordingly used in manufacturing most of the components. However, each individual component of the aircraft requires specific structural properties; hence, the manufacturing method that applies to some parts does not apply to others, and this is why the foam and 3D-printing are inevitably used to manufacture some parts. A more detailed discussion of the four investigated techniques is presented in *table 6.2* below.

Table 6.2: Manufacturing Process Investigation

Method	Discussion
Plywood	Plywood is a stiff light weighted material that can be easily shape and constructed using CNC laser cutting machines and a variety of adhesives. Well-designed and constructed plywood structures increase the overall integrity. Additionally, the fact that the team has a plenty of experience using it made it the perfect choice for manufacturing most of the aircraft parts especially those subjected to a lot of stresses: the fuselage main structure, the tail structure, the mechanism, and so forth.
Foam Core	In this method, large blocks of Polystyrene foam (blue foam) and white foam boards are cut and shaped using CNC hotwire cutting and laser cutting machines. Since this process is simple, it is suitable for rapid prototyping and manufacturing. Furthermore, it is relatively cheap and light in weight. As a result, it has been favored by the team over the years in the majority of the previously manufactured UAVs, and as shown in the table above, it is still favored over the other techniques. Hence, it was decided to rely on it in manufacturing the major components: the wing and the fuselage upper skin.
Balsa Build-Up	In this method, different parts are cut out of balsa wood, by laser-cutting machine and are joined together using cyanoacrylate adhesive. It is known that Balsa wood is optimal for light structure as it is characterized by high-strength-to-weight ratio. Moreover, the team has been using this technique for ten years, and hence has grown more experience using it over the years. The Balsa build-up method, nonetheless, still requires tremendous effort and time in manufacturing and assembly. Moreover, carbon fiber rods, aluminum and plywood will be required for the spars and the main aircraft structure for adding structural strength. Hence, it was excluded this year.
3D Printing	In this method, the CAD model is accurately implemented, where ABS plastic rods are melted and shaped using the 3D printer available at the Cairo university's UDC lab. This process is relatively expensive; it is, however, very simple and reliable. As a result, it will be used to manufacture some parts in the aircraft and the sensor such as the motor mount, the tail assembly connector, and the LED housing units in the sensor.
Composites	In this method, new molds have to be built with each design modification. It is, hence, a very time-consuming method, and the team lacks the enough experience of using it as a reliable method. Moreover, composite materials themselves are very expensive. As can be seen in <i>table 6.1</i> this is the least-scoring technique and its usage was, accordingly, eliminated.

6.2 Selected Manufacturing Process

This section demonstrates, in details, the planned manufacturing process of each part of the aircraft and the payload once the lockdown is over. It was planned to start the manufacturing process back in October, and it should have continued till the end of March; a lockdown in Egypt, however, interfered with the team's plan. Hence, some parts have been already manufactured, and their real images are presented in this section. On the other hand, SolidWorks CAD pictures will be used to represent the parts that have not been manufactured yet.

Wing

The airfoil selected for the wing will be laser-cut from a 0.2-inch-thickness plywood sheet. This plywood template will be used to guide the hot-wire cutter device while cutting each individual semi-span from a 2 in blue polystyrene foam sheets of $1.44 \text{ lb}/\text{ft}^3$ density. 0.12-inch-thickness plywood root ribs will also be laser-cut and attached to the root of each semi-span using hot glue. Two 0.4-inch-diameter aluminum spars will be used to support the wing-fuselage fixation and to bear the flight loads. The wing structure can be illustrated in *figure 6.1*.

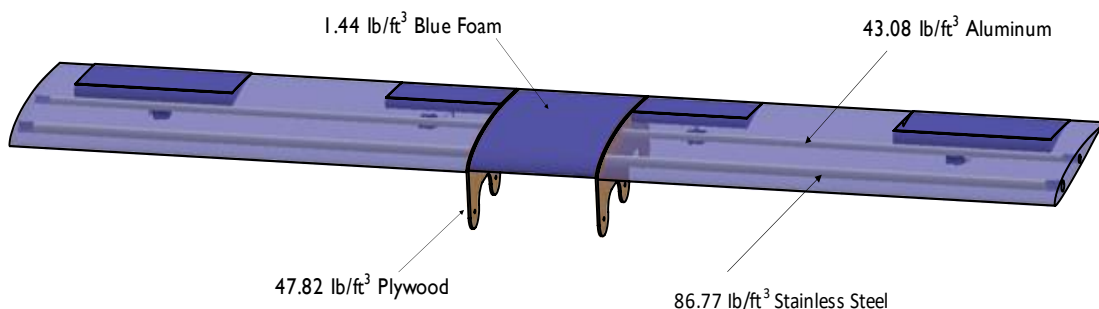


Figure 6.1: Wing and Fuselage Fixation

Tail Structure

The vertical and horizontal tails will be laser-cut into 0.12-inch-thickness plywood sheet. The elevator and rudder will be also laser-cut during the same process and will be connected to the tail using aluminum hinges. A 3D-printed-PLA+ connector will be used to join the vertical tail, horizontal tail, and the fuselage structure. The tail assembly is shown in *figure 6.2*.

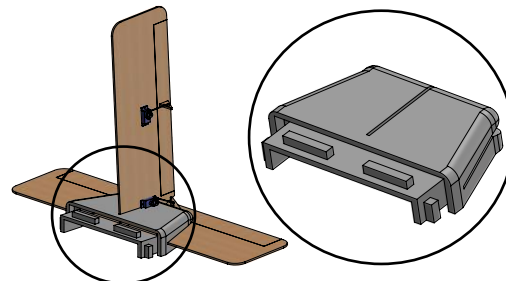


Figure 6.2: Tail Assembly

Deploying/Recovery Mechanism

The mechanism's structure is mainly made of plywood. Individual parts were laser-cut from a 0.12-inch-thickness plywood sheet and joined using super glue. The ratchet wheel pulley was 3D-printed and fixed to the top wall of the sensor compartment using epoxy, as shown in *figure 6.3*.

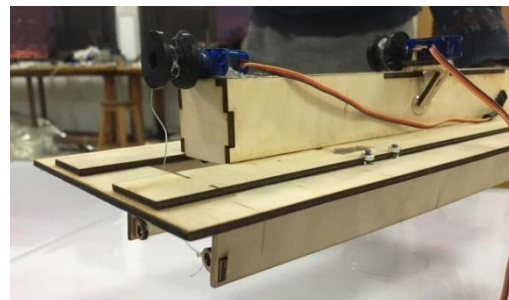
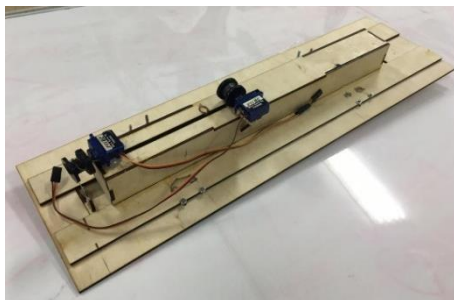


Figure 6.3: Deployment/recovery mechanism

Fuselage

Individual parts of the fuselage structure will be laser-cut from a 5-mm plywood sheet, and the fuselage skin will be cut from a 0.12 in. white-foam sheet of $8.6 \text{ lb}/\text{ft}^3$ density. The structure parts will be assembled using super glue, and the white-foam skin will be attached to it using hot glue. Afterwards, the deploying/recovery mechanism will be glued to the fuselage floor using super glue, and the 3D-printed motor mount will be fitted and screwed to the front openings at the fuselage structure to secure the fixation. Eventually, the fuselage body will be screwed to the plywood root ribs of each semi-span, the tail assembly connector will be fitted to the fuselage rear, and the aluminum landing gear will be screwed to the fuselage floor. The fuselage structure is shown in *figure 6.4*.

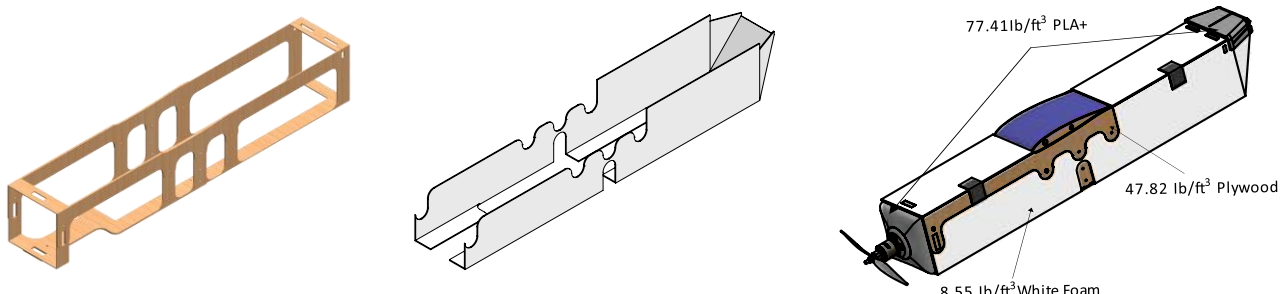


Figure 6.4: Fuselage Structure

The Sensor Shipping Container

The container walls will be cut out from a 0.12-inch-thickness white-foam sheet of $8.6 \text{ lb}/\text{ft}^3$ density. Blue foam supporters will be glued to the top and bottom walls of the container to damp the drop impact and to keep the sensor in its place inside the container. The cut-out white foam walls will be folded and fixed together using hot glue. Eventually, the container will be locked using Velcro strips, as shown in *figure 6.5* below.

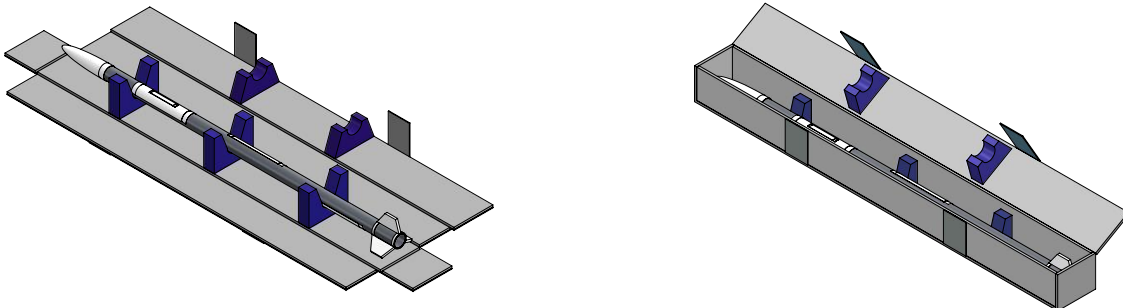


Figure 6.5: The Sensor Fixation Inside its Shipping Container

The Sensor

The sensor main body is made of a 2.5-inch-diameter hollow aluminum cylinders. Three cuts are made in the hollow cylinder and are replaced by 3D-printed-PLA+ units for placing the LEDs. The 3D-printed front cone is attached to the aluminum cylinder using epoxy. Moreover, the three stabilizing fins are also 3D-printed and glued to a 3D-printed-PLA+ ring using epoxy. The stabilizing fins unit is then attached to the sensor main body using epoxy. The designed sensor is illustrated in *figure 6.6*.

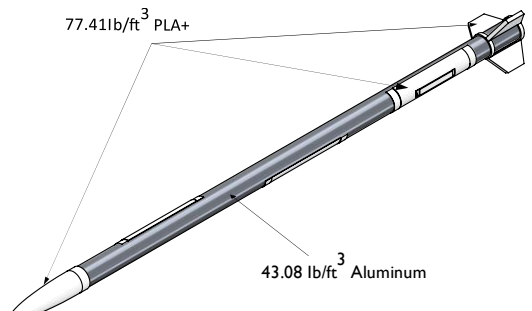


Figure 6.6: The Towed Sensor Structure

6.3 Manufacturing Schedule

The whole prototype manufacturing was planned to be finished in three days to ensure rapid prototyping and efficient lab time usage after the lockdown. The following milestone Gant chart, shown in *figure 6.7*, was made to organize the manufacturing process.

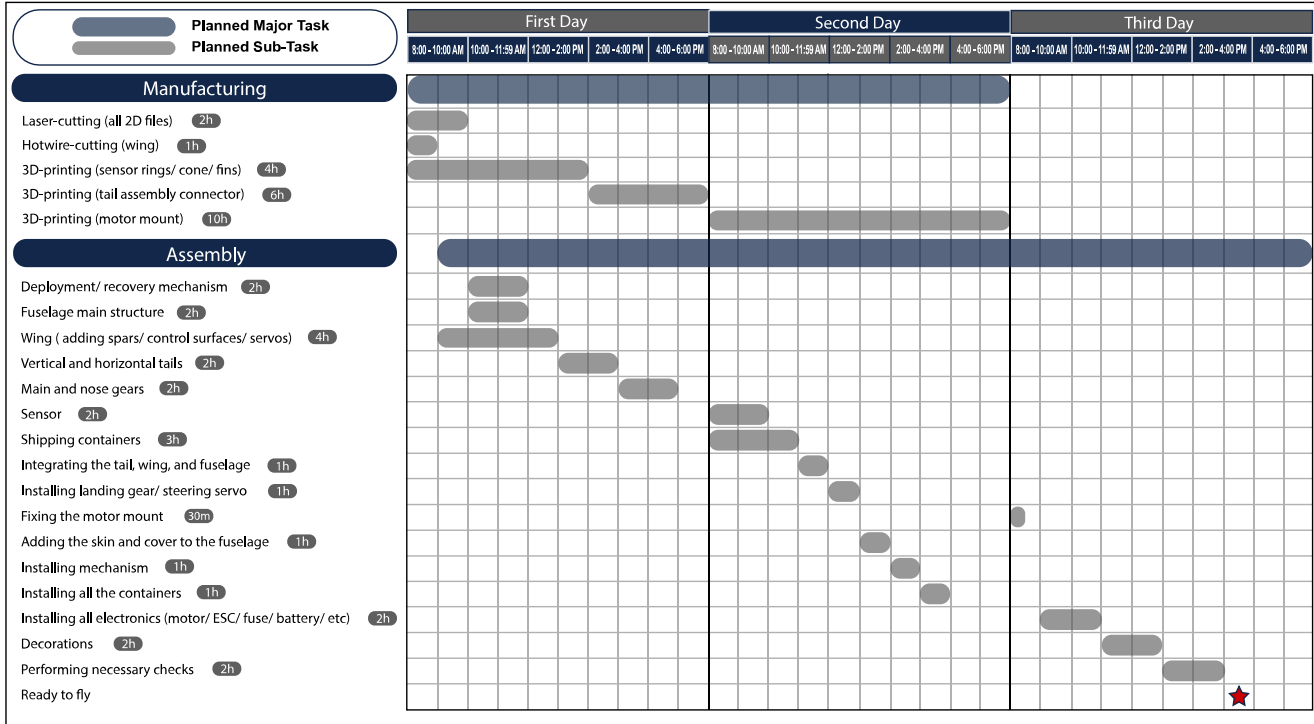


Figure 6.7: Manufacturing Milestone

7.0 Testing Plan

To verify that all subsystems are functioning as proposed and that the aircraft is reliable for completing all flight missions, a comprehensive testing plan, illustrated with the flow chart in *figure 7.1*, was developed. Due to the lockdown period, however, part of the testing process was postponed. Structure and flight testing, in particular, were postponed, and simulations on ANSYS and SolidWorks were used for the shipping container and the landing gear drop test as well as the motor mount test. The propulsion system testing, on the other hand, went as planned and was finished before the lockdown. This section includes the planned steps for the tests once the lockdown is over as well as the simulation setup and the actual propulsion system testing details.

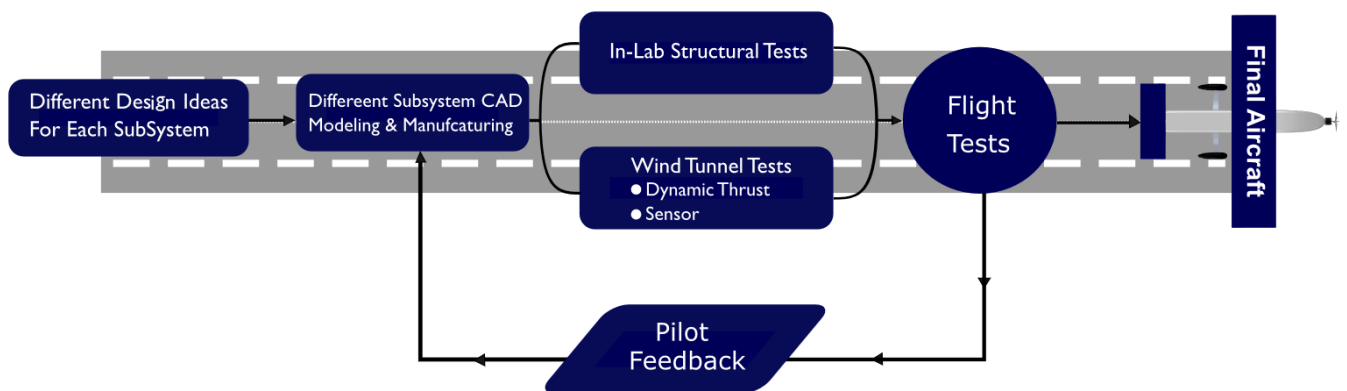


Figure 7.1: Testing Plan Flowchart

7.1 Testing Schedule and Objectives

Figure 7.2 shows the modified compact testing schedule after the lockdown.

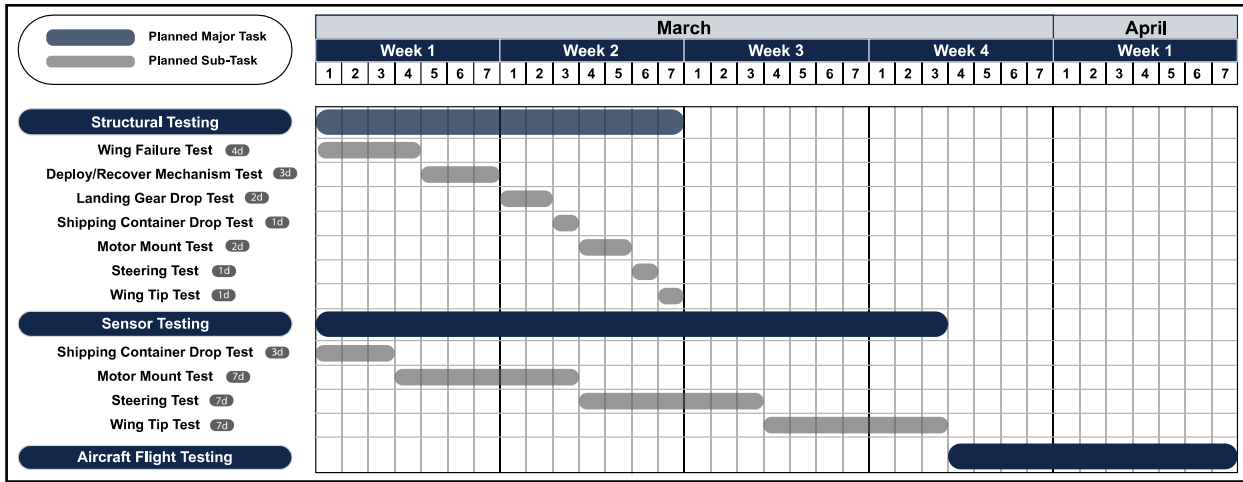


Figure 7.2: Post-Lockdown Testing Schedule

Table 7.1 below provides an overview of the main objectives of each testing phase.

Table 7.1: Testing Objectives

Test	Objective
Propulsion	<ul style="list-style-type: none"> - Validating the static and dynamic thrust calculations and the propulsion system predicted performance - Testing the batteries' discharge rates, capacity, endurance, and performance
Structure	<ul style="list-style-type: none"> - Validating the strength and reliability of the aircraft's structure in bearing the expected loads - Verifying the landing gear impact load endurance - Testing the functionality of the sensor deployment/recovery mechanism.
Flight	<ul style="list-style-type: none"> - Testing the aircraft's controllability and the movement range of the control surfaces - Testing the aircraft's stability in the different flight modes - Confirming the sensor aerodynamic stability in <i>M</i>2 - Validating and optimizing the performance of the aircraft in the flight mission - Calculating and improving the flight missions' score

7.2 Subsystem Testing

7.2.1 Propulsion Testing

The propulsion system, considered in subsection 4.3.2, was tested by the propulsion sub-team to verify the performance estimated in subsection 5.3.8. In order to measure the endurance of the selected batteries, they were discharged at the expected cruising currents using the test set up shown in figure 7.3. The data collected during the test was used to plot the voltage versus time.



Figure 7.3: Batteries Discharge Test

Besides, the batteries were tested using RC benchmark series-1580 to measure their internal resistance at different throttle settings. The plot of the internal resistance with the consumed current, shown in *figure 7.4*, indicates that the actual internal resistance is approximately constant at currents higher than 12 A.

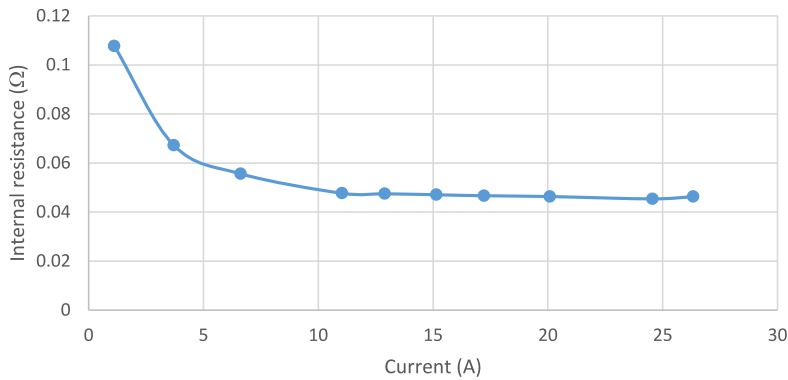


Figure 7.4: The Internal Resistance with the Consumed Current

In order to measure the static thrust, the selected propulsion system of each mission was assembled and tested. The test set up consisted of a static thrust bench and sensitive balance as shown in *figure 7.5*. During the test, the balance readings indicated the available thrust, which was monitored and recorded using a fixed camera. Besides, the SPORTO Platform software was used to record the RPM, the current consumed by the motor and the output power at different throttle settings.

The actual performance of the overall system of *M2* and *M3* was tested in the wind tunnel. A set of sensors was used to measure and record the thrust, drawn current and voltage. The test was conducted for a wide range of velocities. The collected data was curve fitted to get the available thrust versus velocity curve. In *subsection 8.1.1* the obtained results were compared to the values resulting from the sizing framework.

7.2.2 Structure Testing

Wing Testing

A wing bending test will be conducted to validate the structural integrity and reliability of the wing design. The wing spars will be inserted inside the test connector; moreover, the connector will be fixed to a horizontal table using a bench vise or a clamper. *Figure 7.6* shows the test connector fixed to a bench vise to ensure a stable cantilever fixation for the wing.

A laser pen will be mounted at the tip of the wing pointing to a scaled vertical surface to calibrate the deflection. In this test, barbell weights will be used, because they are calibrated; besides, they will simulate a distributed load over the wing. The wing testing setup is illustrated in *figure 7.7* next page.



Figure 7.5: Motor Static Test

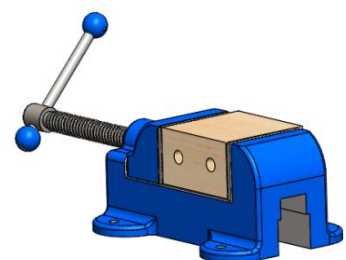


Figure 7.6: The Test Connector

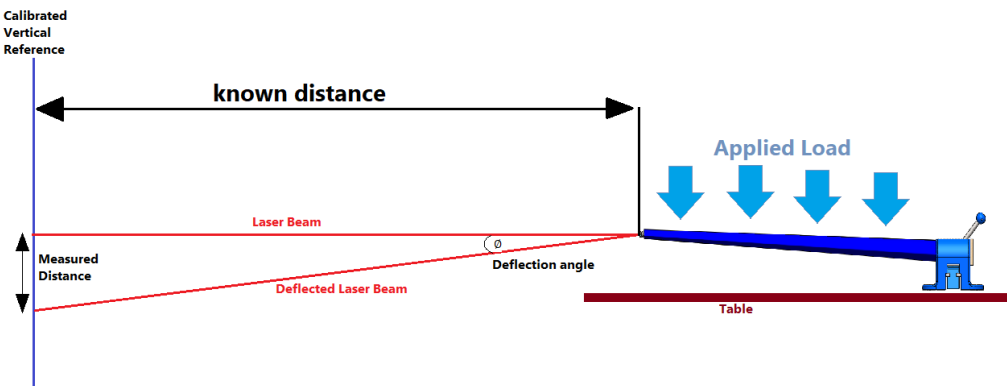


Figure 7.7: Test Setup

Landing Gear Drop-test

The landing gear was subject to a simulated drop test using ANSYS to ensure its endurance of impact loads. It was dropped at a height of 39.37 in. above the concrete-ground. The results of the simulation showed that the landing gear can withstand 22.05 lb. without failure. The deformation is shown in *figure 7.9*.

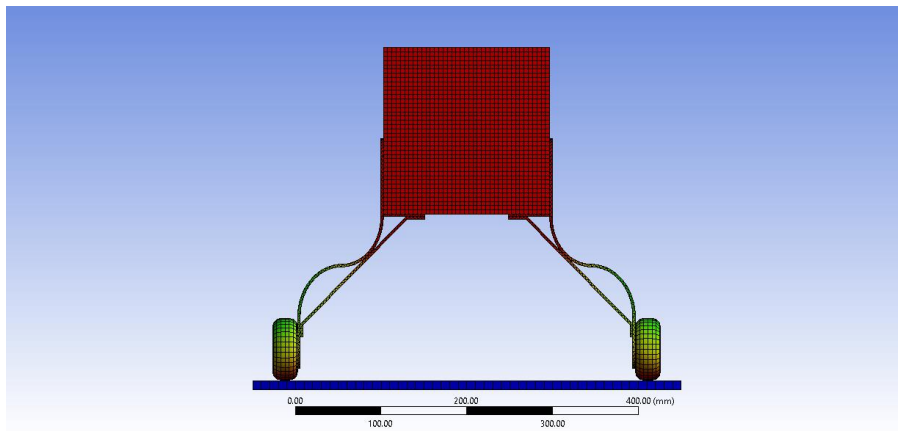


Figure 7.9: The Landing Gear Test Simulation

To verify the results of the simulated drop test, an in-lab test must be done after the lockdown. The test will be conducted using barbell weights added to an extension – manufactured by welding two steel cylinders as shown in *figure 7.8*. The extension will be mounted to the landing gear assembly, and weights will be added to it. Furthermore, weights will increase until the landing gear fails.



Figure 7.8: Landing Gear Test Setup

Motor Mount

Utilizing the SolidWorks FEA tool, the motor mount was tested to ensure that it can withstand the deformation under thrust load, as well as the applied torque. To Apply the simulation, the motor mount's body four extensions were hinged, since the motor mount is attached to the fuselage through four screws. Besides, a maximum thrust force of value 2.65 lb was applied to the area of attaching the propeller. As can be seen in *figure 7.10*, stress was estimated using the von Mises stress criterion, which is a method to determine if a material will yield or fracture. After the analysis, the maximum stress affecting the motor mount is $2.33e2$ psi, which is below the yield stress of PLA+ with a safety factor of 1.5.

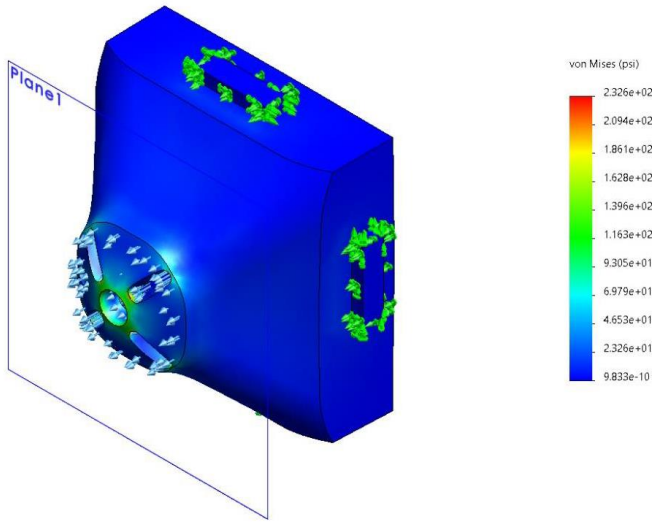


Figure 7.10: FEA of Motor Mount

7.3 Ground Mission Simulation

In order to decrease the time required to perform the ground mission, the assembly crew members will conduct multiple timed simulations. After each one, the feedback of the assembly crew members will be taken into consideration to improve the payload accessibility. In addition, the container will be exposed to a drop test to ensure its ability to protect the sensor. The sensor inside its container will be dropped from a 10-inch height on all the six sides of the container. Afterwards, the sensor and the container will be checked for any physical damage, and the feedback will be used to improve the rigidity and design of the container to damp the drop impact.

Moreover, during the lockdown period a SolidWorks container drop test simulation was performed to evaluate how well the design and material behave when it is exposed to an external impact force. Hence, this provides a more accurate prediction of the actual drop test results which helps in improving the design for a reliable container that can safely protect the sensor. The empty container was dropped at a height of 10 in from the ground. The results showed that the container is capable of protecting the sensor without failure. The deformation is shown in *figure 7.11*.

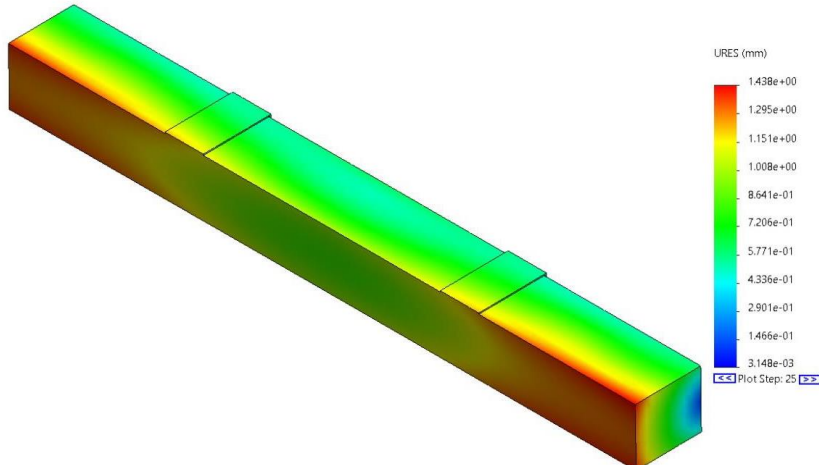


Figure 7.11: FEA of Shipping Container

7.4 Flight Testing

All the flight-related testing will be postponed to mid-March for the official permit. Different flight test schemes are planned for a more efficient feedback and data collection.

- The first flight test will be using a similar aircraft from the previous reliable tested aircrafts in the lab with the sensor and the deployment/recovery mechanism attached to it. Performance will be observed to analyze the impact of the towed sensor on the aircraft in the different flight modes, and to verify the sensor stability during flight.
- The second flight test will be simulating the competition's first flight mission. This year's prototype will be launched and observed to collect and verify data regarding its controllability, response, stability, and its ability to complete the flight course in general.
- The third flight test will be simulating the competition's second flight mission. The aircraft with the payload (sensor in its shipping container, three shipping container simulators, and the deployment recovery mechanism) will be launched and observed. Time for the mission completion will also be recorded and compared for different trials after applying any feedback to modify the prototype.
- The fourth flight test will be simulating the competition's third flight mission. The aircraft with the sensor installed in its mechanism will be launched. The sensor aerodynamic stability will be tested in the flight course. The deployment/recovery mechanism ability to deploy and recover the sensor during the mission shall also be verified. Moreover, the sensor lights visibility will also be tested. With each trial, the number of laps will be recorded.

In each trial, the performance results will be collected to either verify the desired/expected performance or to utilize them along with the pilot's feedback to modify the prototype in order to improve the performance.

7.5 Flight Checklists

The pre-flight checklist, shown in *figure 7.12*, will be used in to ensure the aircraft functionality, the team safety and the data acquisition efficiency. Besides, another checklist, shown in *figure 7.13*, will be used to inspect the aircraft before and after each flight in order to discover any possible problems.

Aircraft Inspection Checklist	
<input type="checkbox"/>	The fuselage is free of cracks
<input type="checkbox"/>	The wing and the tail are free of tears
<input type="checkbox"/>	The propeller is free of cracks
<input type="checkbox"/>	No damage within the landing gear
<input type="checkbox"/>	The sensor is free of fractures
<input type="checkbox"/>	The sensor lights functioning well

Figure 7.13: Aircraft Inspection Checklist

Pre-flight Checklist			
Weather Conditions	<input type="checkbox"/> Sunny	<input type="checkbox"/> Windy	<input type="checkbox"/> Rains
Wind Speed	<input type="text"/>		
<input type="checkbox"/> Secure all fasteners <input type="checkbox"/> Secure the motor mount <input type="checkbox"/> Secure the charged batteries <input type="checkbox"/> Plug in and secure the receiver <input type="checkbox"/> Load and secure the shipping containers (Mission 2) <input type="checkbox"/> Secure the sensor deploying & recovery mechanism (Mission 3) <input type="checkbox"/> Close the aircraft hatches <input type="checkbox"/> Check the C.G location <input type="checkbox"/> Check all the control surfaces <input type="checkbox"/> Go Decision			
Pilot's Feedback: _____			
<input type="text"/> <input type="text"/> <input type="text"/>			
Pilot's Signature: _____			

Figure 7.12: The Pre-flight Checklist

8.0 Performance Results

8.1 Demonstrated Performance of Key Subsystems

8.1.1 Propulsion System

Battery

The selected LiPo battery packs were tested to ensure their ability to endure the 10-minute flight window. Using a test bench, the battery packs were discharged at 80% throttle setting, and the voltage readings were recorded with time. *Figure 8.1* shows the voltage readings versus time in seconds. It is found that the battery packs can maintain the voltage for ten minutes at 34 A. However, this test did not take the headwind effect into consideration.

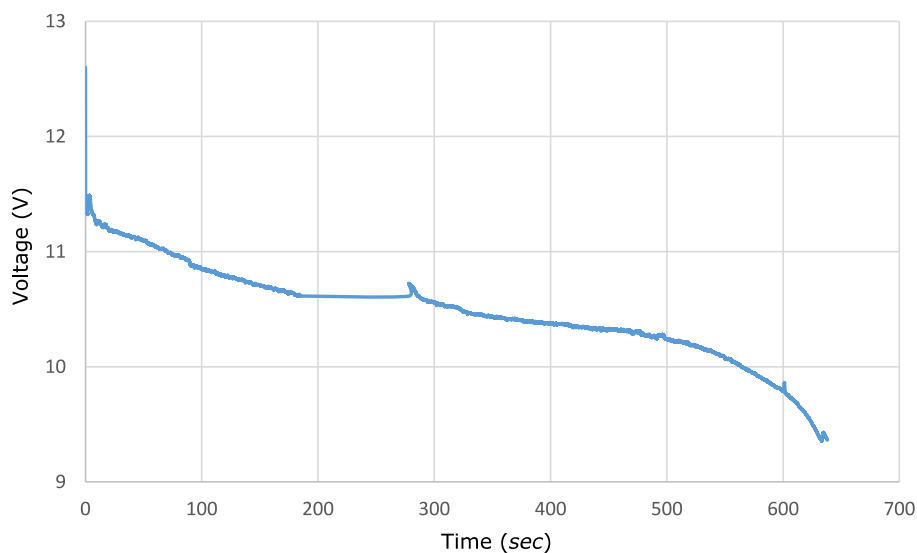


Figure 8.1: The Discharge Curve of 6 Cells LiPo Battery Pack (6000 mAh) at 34A

Motor & Propeller Combination

- *Static Testing*

The combinations of each mission, which were selected by the way discussed in *subsection 4.3.2*, were tested to measure the static thrust. *Figure 8.2* compares between the expected and actual static thrust for each mission.

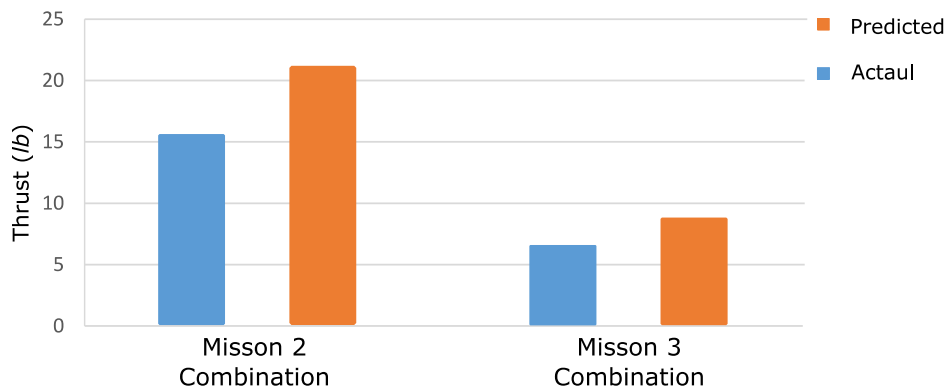


Figure 8.2: Predicted and Actual Static Thrust for M2 and M3

- *Dynamic Testing*

The selected propulsion system was prepared to be tested in the wind tunnel, as mentioned in section 5.3.8. Figure 8.3 compares between the actual thrust and the predicted thrust resulting from the MATLAB framework.

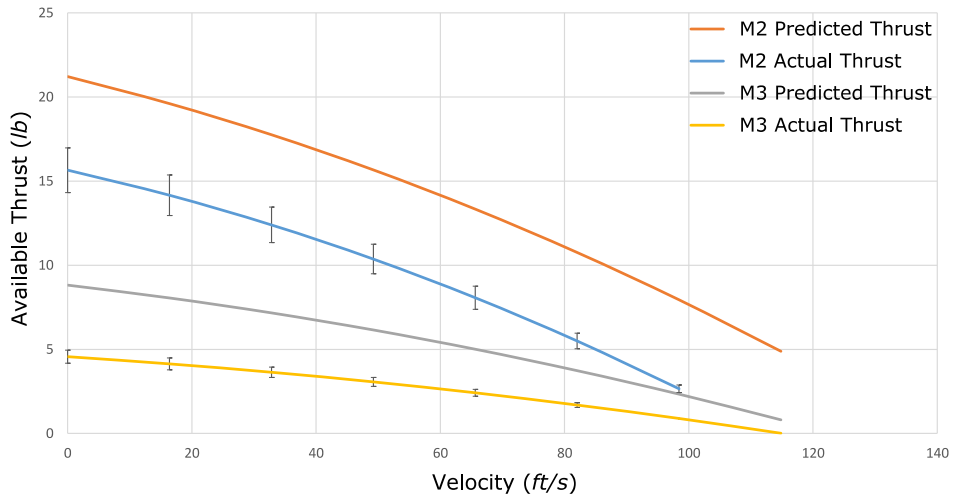


Figure 8.3: Predicted and Actual Dynamic Thrust for M2 and M3

Eventually, the difference between the predicted and the measured performance of the propulsion system was acceptable. Therefore, the code results were considered reasonably accurate without further improvements.

9.0 Bibliography

- [1] J. D. Anderson, *Introduction to Flight*, 7th ed., McGraw-Hill Science/Engineering/Math, 2011.
- [2] L. Scientific, "Lab Rockets and Space Page," [Online]. Available: http://www.labratscientific.com/Rockets_and_Space_Page.html. [Accessed 2020].
- [3] D. P. Raymer, *Aircraft Design: A Conceptual Approach*, 2nd ed., American Institute of Aeronautics and Astronautics, 1992.
- [4] M. H. Sadraey, *Aircraft Design: A Systems Engineering Approach*, 1st ed., John Wiley & Sons Ltd, 2013, pp. 655-671.
- [5] A. Sóbester, A. Keane and J. P. Scanlan, *Small Unmanned Fixed-wing Aircraft Design: A Practical Approach*, 1st ed., John Wiley & Sons Ltd, 2017.
- [6] AIAA Student Design Build Fly, "2020-21 Design/Build/Fly Q&A #1," 2021. [Online]. Available: <https://www.aiaa.org/dbf/competition-information/QA>.
- [7] R. C. Nelson, *Flight Stability and Automatic Control*, 2nd, Ed., New York: McGraw-Hill, 1998.
- [8] G. Staples, "Propeller Static and Dynamic Thrust Calculation," 12 April 2012. [Online]. Available: <https://www.electricrcaircraftguy.com/2014/04/propeller-static-dynamic-thrust-equation-background.html>. [Accessed 2020].
- [9] S. Gudmundsson, *General Aviation Aircraft Design: Applied Methods and Procedures*, Elsevier Inc., 2014.
- [10] J. Gundlach, *Designing Unmanned Aircraft Systems: A Comprehensive Approach*, 2nd ed., Reston, VA: American Institute of Aeronautics and Astronautics.